

1      **New constraints from  $^{26}\text{Al}$ - $^{26}\text{Mg}$  chronology of anorthite bearing**  
2      **chondrules in unequilibrated ordinary chondrites**

3

4      Guillaume Siron<sup>a</sup>, Kohei Fukuda<sup>a</sup>, Makoto Kimura<sup>b</sup>, and Noriko T. Kita<sup>a</sup>

5

6      <sup>a</sup> WiscSIMS, Department of Geoscience, University of Wisconsin-Madison, Madison, WI 53706,  
7      USA

8      <sup>b</sup> National Institute of Polar Research, Meteorite Research Center, Midoricho 10-3, Tachikawa,  
9      Tokyo 190-8518, Japan

10

11     corresponding author: siron@wisc.edu

12

13

## ABSTRACT

14

15  $^{26}\text{Al}$ - $^{26}\text{Mg}$  ages were determined for 14 anorthite-bearing chondrules from five different  
16 unequilibrated ordinary chondrites (UOCs) with low petrologic subtypes (3.00-3.05). In addition,  
17 oxygen three isotopes of these chondrules were also measured. The selected chondrules are highly  
18 depleted in alkali elements, and anorthite is the only mesostasis phase, though they show a range  
19 of mafic mineral compositions (Mg# 76-97 mole%) that are representative of chondrules in UOCs.  
20 The mean  $\Delta^{17}\text{O}$  values in these chondrules range from  $-0.44 \pm 0.23\text{\textperthousand}$  to  $0.49 \pm 0.15\text{\textperthousand}$ , in good  
21 agreement with previous studies of plagioclase-bearing chondrules from UOCs. Anorthite in all  
22 chondrules exhibit resolvable excess  $^{26}\text{Mg}$  ( $> 1.0 \pm 0.4\text{\textperthousand}$ ). Their inferred  $(^{27}\text{Al}/^{26}\text{Al})_0$  range from  
23  $(6.3 \pm 0.7) \times 10^{-6}$  to  $(8.9 \pm 0.3) \times 10^{-6}$  corresponding to a timescale for chondrule formation of  $1.8 \pm$   
24  $0.04$  Ma to  $2.16 \pm ^{0.12}_{0.11}$  Ma after CAIs using a canonical  $(^{27}\text{Al}/^{26}\text{Al})_0$  value of  $5.25 \times 10^{-5}$ . The  
25 ages from six chondrules in LL chondrites are restricted to between 1.8 Ma and 1.9 Ma, whereas  
26 eight chondrules in L chondrites show ages from 1.8 Ma to 2.2 Ma, including three chondrules at  
27  $\sim 2.0$  Ma and two chondrules at  $\sim 2.15$  Ma.

28 The inferred chondrule formation ages from this study are at the peak of those previously  
29 determined for UOC chondrules, though with much shorter durations. This is potentially due to  
30 the time difference between formation of anorthite-bearing chondrules and typical UOC  
31 chondrules with alkali-rich compositions. Alternatively, younger chondrules ages in previous  
32 studies could have been the result of disturbance to the Al-Mg system in glassy mesostasis even at  
33 the low degree of thermal metamorphism in the parent bodies. Nevertheless, the high precision  
34 ages from this study (with uncertainties from 0.04 Ma to 0.15 Ma) indicate that there was  
35 potentially more than one chondrule forming event represented in the studied population.

36 Considering data from LL chondrites only, the restricted duration ( $\leq 0.1$  Ma) of chondrule  
37 formation ages suggests an origin in high density environments that subsequently lead to parent  
38 body formation. However, the unusually low alkali contents of the studied chondrules compared  
39 to common alkali-rich chondrules could also represent earlier chondrule formation events under  
40 relatively lower dust densities in the disk. Major chondrule forming events for UOCs might have  
41 postdated or concurrent with the younger anorthite-bearing chondrule formation at 2.15 Ma after  
42 CAIs, which are very close to the timing of accretion of ordinary chondrite parent bodies that are  
43 expected from thermal evolution of ordinary chondrite parent bodies.

44

45

## 1. INTRODUCTION

46

47 Chondrules, one of the main components of chondrites, represent solidified melt droplets  
48 resulting from transient high temperature heating of dust aggregates in the protoplanetary disk  
49 (Grossman, 1988; Jones, 2012). Shock-wave heating is the most developed model of chondrule  
50 formation, though the detailed mechanisms of chondrule formation has been a controversial  
51 subject for decades (Desch et al., 2012). The timing and duration of chondrule formation are the  
52 keys to constrain the mechanism(s) of chondrule formation and help us to understand the evolution  
53 of the early Solar System. Indeed, studies suggest that chondrules in ordinary chondrites (OCs),  
54 which would have formed under high dust density disk environments, should show a very short  
55 period of formation ages (i.e., < 0.1 Ma) due to subsequent planetesimal formation (Alexander,  
56 2005; Alexander et al., 2008; Alexander and Ebel, 2012). Such short timescales would prevent any  
57 large-scale mixing of materials in the protoplanetary disk (Cuzzi et al., 2010). The two most  
58 commonly used chronometers for chondrule formation ages are the  $^{207}\text{Pb}$ - $^{206}\text{Pb}$  system (Connelly  
59 et al., 2012; Bollard et al., 2017) and the  $^{26}\text{Al}$ - $^{26}\text{Mg}$  system (Hutcheon and Hutchison, 1989;  
60 Hutcheon and Jones, 1995; Kita et al., 2000; Villeneuve et al., 2009; Kita and Ushikubo, 2012). In  
61 contrast to the prediction of a short time interval (0.1 Ma) for the formation of UOC chondrules  
62 (Alexander and Ebel, 2012), most studies indicate that UOC chondrule formation occurred 0-4 Ma  
63 and 1.5-3 Ma after Ca, Al-rich inclusions (CAIs) for Pb-Pb and Al-Mg ages, respectively (e.g.,  
64 Bollard et al., 2017; Pape et al., 2019). It is important to note that the ages obtained from these two  
65 methods represent the timing for their last melting event (Kita and Ushikubo, 2012; Bollard et al.,  
66 2017; 2019).

67 The  $^{26}\text{Al}$ - $^{26}\text{Mg}$  system applied to chondrule chronology is a powerful tool because of its  
68 short half-life ( $7.05 \times 10^5$  years after Nishiizumi, 2004). This allows for the precise determination  
69 of ages within a few million years of the formation of the oldest solids in the Solar System, CAIs  
70 (Kita et al., 2013). Due to the relatively low initial ratio of  $(^{26}\text{Al}/^{27}\text{Al})_0$  in chondrules ( $\leq 10^{-5}$ )  
71 compared to CAIs ( $5 \times 10^{-5}$ ), earlier in-situ secondary ion mass spectrometry (SIMS) analyses were  
72 conducted on Al-rich chondrules (Hutcheon and Jones, 1995; Russell et al., 1996; Russell et al.,  
73 1997) and one “clast chondrule” that contain coarse anorthite (Hutcheon and Hutchison, 1989).  
74 More recently, several studies have constrained the  $^{26}\text{Al}$ - $^{26}\text{Mg}$  ages of ferro-magnesian chondrules  
75 in unequilibrated ordinary chondrites (UOCs), either using high primary current (Villeneuve et al.,  
76 2009; Pape et al., 2019) or a smaller spot size (Kita et al., 2000; Mostefaoui et al., 2002;  
77 Rudraswami and Goswami, 2007; Rudraswami et al., 2008; Bolland et al., 2019). The higher count  
78 rates obtained by the first method allows the use of high precision multi-collection Faraday cup  
79 (MCFC) analyses. This works well for many UOC chondrules because most contain glassy  
80 mesostasis with low  $^{27}\text{Al}/^{24}\text{Mg}$  ratios and relatively small excesses in  $^{26}\text{Mg}$ . On the other hand,  
81 analyses using a small spot size can avoid beam overlap between high-Ca pyroxene and  
82 mesostasis, and also make it possible to target phases with high  $^{27}\text{Al}/^{24}\text{Mg}$  ratios that have larger  
83 excess  $^{26}\text{Mg}$ . These analyses can provide important constraints despite the lower precision  
84 associated with lower counts for Mg isotopes. Results from these two different approaches give  
85 significantly different durations for chondrule formation. The first approach yields a long duration  
86  $\sim 1.5$  Ma over which chondrule formation occurred, a range that is greater than analytical  
87 uncertainties for each chondrule age (Villeneuve et al., 2009; Pape et al., 2019), whereas the second  
88 indicates a more restricted duration  $\sim 0.4$  Ma that is comparable to the uncertainties on individual  
89 chondrule ages (Kita et al., 2000). Alexander and Ebel (2012) suggested that UOC chondrules

90 would have a limited range of formation ages and proposed that the larger range observed by  
91 Villeneuve et al. (2009) may represent the disturbance of the Al-Mg system due to parent body  
92 metamorphism and/or result from mixed analyses between mesostasis and high-Ca pyroxene. The  
93 SIMS Al-Mg analyses using large analytical spots that overlap high Al/Mg mesostasis (glass and  
94 plagioclase) and mafic minerals would produce mixing line in the isochron diagram, which would  
95 not allow for the assessment of a possible disturbance of the isochron.

96 This paper aims to establish the true range of OC chondrule formation ages and constrain  
97 the formation mechanism of chondrules in OCs. In order to eliminate the potential disturbance of  
98 the Al-Mg system, we selected coarse-grained anorthite-bearing chondrules from several L/LL  
99 3.00-3.05 UOCs for Al-Mg analyses, though anorthite-bearing chondrules are uncommon in UOCs  
100 (Kita et al., 2000; 2010). Experimental data for Mg self-diffusion in anorthite indicates that the Al-  
101 Mg system in anorthite should not be disturbed in the subtypes 3.00-3.05 UOCs that have  
102 experienced limited degrees of metamorphism (Van Orman et al., 2014). In order to obtain reliable  
103 SIMS data, we restricted the primary beam size so that analyses did not overlap adjacent phases  
104 as in our previous study (Kita et al., 2000).

105 These analyses were performed with our upgraded primary radiofrequency (RF) oxygen  
106 plasma ion source that allows us to use smaller and denser primary beams for Al-Mg isotope  
107 analyses (Hertwig et al., 2019). Furthermore, modifications of the detection system for lower Mg  
108 secondary ion intensities ( $\leq 10^6$  cps) significantly improve the analytical precision by: (1) reduction  
109 of MCFC thermal noise by using high gain feedback resistor ( $10^{12}$  ohm; Fukuda et al., 2020) and  
110 (2) improvements in counting statistics by using multi-collector electron multiplier (MCEM) pulse  
111 counting system (Kita et al., 2018; Hertwig et al., 2019).

112

113

## 2. METHODS

114

### 115 2.1 Samples

116

117 The UOCs selected for this study have all been classified as subtypes 3.00-3.05 from their  
118 Cr<sub>2</sub>O<sub>3</sub> contents in fayalitic olivine (Grossman and Brearley, 2005). The sections studied here are  
119 as follows; Semarkona (LL3.00) polished thin section (PTS) USNM 1805-9, polished mounts of  
120 NWA 8276 (L3.00) and NWA 8649 (LL3.05) from University of New Mexico, and QUE 97008  
121 (L3.05) PTS #12 and MET 00452 (L/LL 3.05) PTS #16 from US Antarctic meteorite program  
122 (ANSMET). Classification of MET 00452 is from its pair MET 00526 (L/LL3.05; Grossman and  
123 Brearley, 2005). Semarkona was classified as LL3.01 based on Fe-Ni metal (Kimura et al., 2008)  
124 that is sensitive to low degree thermal metamorphism between 3.00-3.10. According to Fe-Ni  
125 metal observations (Kita et al., 2019), NWA 8276 seems to be slightly more metamorphosed than  
126 Semarkona and similar to other 3.05 UOCs studied here. Semarkona has low shock stage S2, and  
127 MET 00452, MET 00526, QUE 97008, and NWA 8649 were described as low shock. No  
128 information for shock stage is known for a paired meteorites NWA 7731 and NWA8276, though  
129 we do not recognize any obvious shock features.

130

### 131 2.2. Electron microscopy

132

133 Backscattered secondary electron (BSE) and secondary electron (SE) images were  
134 acquired using a Hitachi 3400 variable pressure scanning electron microscope (SEM). More than  
135 800 chondrules from multiple UOC sections were examined using EDS spectra and BSE images

136 in order to search chondrules that contain coarse grained anorthite ( $\geq 10 \mu\text{m}$ ) large enough to  
137 analyze with the  $6 \mu\text{m}$  SIMS spot.

138 Major and minor element analyses were obtained using electron probe microanalyzers  
139 (EPMA) at the Eugene Cameron Electron Microprobe Laboratory of the University of Wisconsin-  
140 Madison using 15 kV and 15 nA beam conditions. Plagioclase analyses were obtained during three  
141 different sessions. The first and 3<sup>rd</sup> sessions used the Cameca SX5 Field Emission gun microprobe  
142 using a beam size of  $3 \mu\text{m}$ , the 2<sup>nd</sup> session used the Cameca SX51 microprobe with a beam size of  
143  $5 \mu\text{m}$ , both are equipped with five wavelength dispersive spectrometers. Counting times were 10  
144 seconds on the wavelength peak and 5 seconds on both backgrounds, except for the second session  
145 where Al and Ti were measured using the mean atomic number (MAN) method (Donovan et al.,  
146 2016), for which no background is required. During this second session, counting times were  
147 reduced for Na, K and Mn to 5 seconds on both backgrounds and peak and increased to 20 (peak)  
148 and 10 (backgrounds) seconds for Mg. Albite for Na and Si, anorthite for Ca and Al, microcline  
149 for K, hematite (1<sup>st</sup> session) or BHVO glass (2<sup>nd</sup> and 3<sup>rd</sup> session) for Fe, forsterite (1<sup>st</sup> session) or  
150 andesite glass (2<sup>nd</sup> and 3<sup>rd</sup> sessions) for Mg, Cr<sub>2</sub>O<sub>3</sub> oxide for Cr, Mn-olivine for Mn and TiO<sub>2</sub> oxide  
151 for Ti served as standards. Olivine and pyroxenes were analyzed using a  $3 \mu\text{m}$  beam size. The  
152 same counting times as in the third session of plagioclase analyses were used. The following  
153 standards were used for olivine: Mg-olivine (Mg, Si), augite (Ca), anorthite (Al), hematite (Fe),  
154 Cr<sub>2</sub>O<sub>3</sub> oxide (Cr), Mn-olivine (Mn) and TiO<sub>2</sub> oxide (Ti). The following standards were used for  
155 pyroxenes: enstatite (Mg, Si), augite (Ca), anorthite (Al), hematite (Fe), Cr<sub>2</sub>O<sub>3</sub> oxide (Cr), Mn-  
156 olivine (Mn) and TiO<sub>2</sub> oxide (Ti). All elements were far above detection limits, except TiO<sub>2</sub> and  
157 Na<sub>2</sub>O that had detection limits of 0.030 wt.% and 0.015 wt.%, respectively.

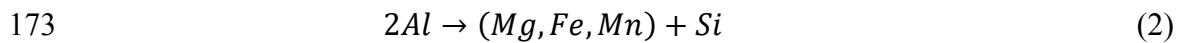
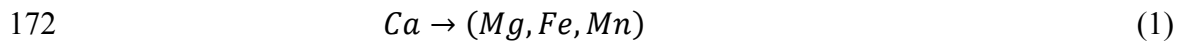
158 No differences were found between glass and mineral standards for major and trace  
159 elements between the different sessions. Notably, MgO contents were between 0.5-1 wt.% for pure  
160 anorthite (i.e., > An<sub>93</sub> in this study; where An = Ca / (Ca + Na + K) mol%). The data were reduced  
161 using the Probe software package using both ZAF and  $\phi_{pz}$  matrix correction routines. In this paper,  
162 all uncertainties for major and minor elements are one standard deviation (1SD).

163

164 *2.2.2 Plagioclase end-member determination*

165 Anorthite-rich plagioclase in chondrules from the least metamorphosed chondrites  
166 typically contain high MgO (0.5-1%; Kita et al., 2000; Kurahashi et al., 2008), distinctly higher  
167 than from what is found in terrestrial and extraterrestrial igneous rocks. The most striking  
168 differences are their high MgO, FeO, and MnO contents, that can reach up to ~2 wt.% combined  
169 (MacPherson and Huss, 2005). These high contents of divalent cations can be incorporated into  
170 the plagioclase structure by two different substitutions:

171

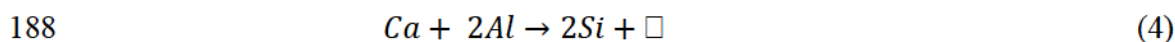
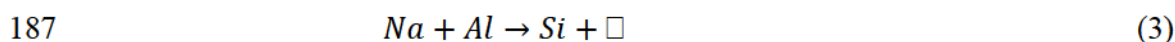


174

175 It is unclear whether these divalent cations enter the plagioclase structure with one or the  
176 other substitutions and it seems to depend on the samples analyzed (Beaty and Albee, 1980).  
177 Nevertheless, there seems to be a preference for substitution (2) to explain the incorporation of Fe,  
178 Mg and Mn cations. This is especially well delineated in lunar samples (Wenk and Wilde, 1973;  
179 Longhi et al., 1976; Beaty and Albee, 1980).

180 Additionally, it has been documented that plagioclase grains from extraterrestrial samples  
181 exhibit excess structural silica ( $\square\text{Si}_4\text{O}_8$ ), especially in lunar samples (Weil et al., 1970; Wenk and  
182 Wilde, 1973; Bruno and Facchinelli, 1975; Beaty and Albee, 1980; Anon, 2014), but also recently  
183 in plagioclase bearing chondrules in CR and Acfer 094 (Tenner et al., 2019) and in Pasamonte  
184 eucrite (Mittlefehldt and Berger, 2017). The incorporation of excess silica follows two substitution  
185 from albite and anorthite endmember:

186



189

190 The proportion of the different plagioclase endmembers are computed using linear algebra,  
191 as described in Thompson (1982) and Spear, Rumble and Ferry (1982):

192

$$193 \qquad \qquad \qquad Ax = b \qquad \qquad \qquad (5)$$

194

195 where A represents the matrix for the stoichiometry of each endmember, with rows  
196 representing the stoichiometry for each element of the endmembers (vectors), x is the vector of the  
197 different proportions of endmembers and b is the measured contents for each cation. Taking into  
198 account all possible endmember, it takes the form of:

199

$$\begin{matrix}
 200 & \begin{bmatrix} 0 & 1 & 0 & 0 & 0 & 0 & 0 & 0 & 0 & 0 \\ 1 & 0 & 0 & 0 & 0 & 0 & 1 & 1 & 1 & 0 \\ 0 & 0 & 1 & 0 & 0 & 0 & 0 & 0 & 0 & 0 \\ 1 & 0 & 0 & 1 & 0 & 0 & 1 & 0 & 0 & 0 \\ 0 & 0 & 0 & 0 & 1 & 0 & 0 & 1 & 0 & 0 \\ 0 & 0 & 0 & 0 & 0 & 1 & 0 & 0 & 1 & 0 \\ 2 & 1 & 1 & 2 & 2 & 2 & 0 & 0 & 0 & 0 \\ 2 & 3 & 3 & 2 & 2 & 2 & 3 & 3 & 3 & 4 \end{bmatrix} \bullet \begin{bmatrix} CaAl_2Si_2O_8 \\ NaAlSi_3O_8 \\ KAlSi_3O_8 \\ CaAl_2Si_2O_8 \\ MgAl_2Si_2O_8 \\ FeAl_2Si_2O_8 \\ MnAl_2Si_2O_8 \\ CaMgSi_3O_8 \\ CaFeSi_3O_8 \\ CaMnSi_3O_8 \\ [ ]Si_4O_8 \end{bmatrix} = \begin{bmatrix} Na \\ Ca \\ K \\ Mg \\ Fe \\ Mn \\ Al \\ Si \end{bmatrix} & (6)
 \end{matrix}$$

201

202        The coefficients for the different proportions of the endmembers is computed using non-  
 203 negative least square fitting, with the target variable being the measured cations. In general, the  
 204 results of this method have been in agreement with the previously used method from Beaty and  
 205 Albee (1980). This method has the advantage of forbidding any negative values for endmembers,  
 206 which would result in the overestimation of the other endmembers. It is especially true when  
 207 plagioclases have low  $\square Si_4O_8$  and  $(Mg,Fe,Mn)Al_2Si_2O_8$  compositions. It can be applied for low Ti  
 208 and Cr content plagioclases since it does not take into account these two cations.

209

210

211 **2.3. SIMS oxygen three isotopes analyses**

212

213        Oxygen three isotope measurements were conducted in a single session using the IMS1280  
 214 at the WiscSIMS laboratory of the University of Wisconsin-Madison. Analytical conditions are  
 215 similar to those described in Kita et al. (2010) and use MCFC for the three isotopes. A focused  
 216 gaussian  $Cs^+$  primary beam at  $\sim 2$  nA was used in order to achieve counts per second (cps) in the  
 217 range of  $(2-3) \times 10^9$  for  $^{16}O^-$ , the spot size was about  $12 \times 10 \mu m$  in diameter. A mass resolving

218 power (MRP) of  $\sim$ 5000 was achieved in order to separate the isobaric interference of  $^{16}\text{O}^1\text{H}$  to  $^{17}\text{O}$ .  
219 The  $^{17}\text{O}$  isotope signal was measured using a Faraday cup (FC) detector with a  $10^{12} \Omega$  resistance  
220 for improved precision. The  $^{16}\text{O}$  and  $^{18}\text{O}$  isotope signals were measured with FC detectors of  $10^{10}$   
221 and  $10^{11} \Omega$ , respectively. Additionally,  $^{16}\text{O}^1\text{H}$  was measured at the end of each measurement to  
222 estimate potential tailing effect on  $^{17}\text{O}$  counts. As in the previous studies, 12-16 unknown  
223 chondrule analyses are bracketed by 8 analyses of SC-Ol standard (e.g., Hertwig et al., 2018). A  
224 slight drift for both  $\delta^{18}\text{O}$  and  $\delta^{17}\text{O}$  standard data (EA1) was recognized during this session, which  
225 should be carefully treated for UOC chondrule data where variabilities in  $\Delta^{17}\text{O}$  are relatively small  
226 ( $\leq 1\text{\textperthousand}$ ; Kita et al., 2010). Thus, we applied a drift correction to the entire dataset using repeated  
227 analyses of the SC-Ol running standard, instead of a simple correction by a set bracket standard  
228 analyses (e.g., Kita et al., 2010). In order to correct the drift during the entire 54 hours of the  
229 analyses, we divided the session into three sections based on the evolution of SC-Ol data with time  
230 (see, EA1). The first section did not require a drift correction, while the second section required  
231 using a 3<sup>rd</sup> order polynomial fit for both  $\delta^{18}\text{O}$  and  $\delta^{17}\text{O}$  and the last section required a 2<sup>nd</sup> order  
232 polynomial fit for  $\delta^{18}\text{O}$  and a linear fit for  $\delta^{17}\text{O}$ . P-values of each coefficient were checked to  
233 achieve a good fit (EA1). The reproducibilities of the SC-Ol standard measurements were typically  
234 0.2‰ for  $\delta^{18}\text{O}$ , 0.25‰ for  $\delta^{17}\text{O}$  and 0.25‰ for  $\Delta^{17}\text{O}$ , after drift correction.

235 Five additional olivine standards (from Fo<sub>60</sub> to Fo<sub>100</sub>), three low-Ca pyroxene standards  
236 (Mg# 0.7-0.97) and one diopside standard (Kita et al., 2010; Fukuda et al., 2020) were analyzed at  
237 the beginning of the session to correct matrix effects depending on the mineral compositions. In  
238 this analysis session, the instrumental biases among olivine standards were nearly the same  
239 ( $\leq \pm 0.3\text{\textperthousand}$ ) within the range of compositions (EA1), so that no additional bias correction depending  
240 on Fo contents was applied. We typically find 0.5-1‰ changes among these olivine standards (e.g.,

241 Tenner et al., 2015), which may change depending on primary beam conditions. This finding is  
242 not surprising since many studies have demonstrated that most of the matrix effect for the olivine  
243 solid solution occur in Fe-rich compositions below Fo<sub>50</sub> (Valley and Kita, 2009; Isa et al., 2017).  
244 Similarly, no significant matrix effect was found for low-Ca pyroxenes standards for such a limited  
245 range of Mg# (70-97 mole%). Correction of matrix effects for Ca content was achieved using the  
246 diopside standard. Additionally, one anorthite standard was used to correct for instrumental bias  
247 for plagioclases analyses.

248 This session showed a small mass dependent fractionation within individual analyses so  
249 instead of using the 2SE we use the 2SD of standard bracket measurements for unknown analyses.  
250 Uncertainties for each individual analysis were estimated by propagating the 2SD of the standard  
251 measurements bracketing the analysis, the 2SE of these standard analyses, the uncertainty on the  
252 fit (95% confidence interval) when corrected for drift and an additional factor of 0.3‰ to account  
253 for the error on the reference values for standards from laser fluorination. The host chondrule O  
254 isotopic compositions were computed following the procedure established in Ushikubo et al.  
255 (2012) and Tenner et al. (2013). During this session, the 3SD for  $\Delta^{17}\text{O}$  of the SC-OI of all  
256 measurements was 0.43‰. In a first step, a mean  $\Delta^{17}\text{O}$  value, including all the analyses for a  
257 chondrule, was computed and analyses that are outside of 3SD (0.43‰) from the mean were  
258 identified. Data were rejected if the remainder of the analyses were all within 3SD limit of their  
259 mean value. The remaining analyses are used to compute the mean oxygen isotope ratios (for  $\delta^{18}\text{O}$ ,  
260  $\delta^{17}\text{O}$ , and  $\Delta^{17}\text{O}$ ), which were assumed to be those of host chondrules. Anorthite analyses were not  
261 used to compute host chondrule compositions. Similarly to individual analyses, the uncertainty on  
262 the host chondrule composition for each chondrule is the propagation of 2SE of all individual

263 measurements inside one chondrule, along with the additional uncertainties in the instrumental  
264 mass fractionation; 0.3‰ and 0.15‰, for  $\delta^{18}\text{O}$  and  $\delta^{17}\text{O}$ , respectively (Kita et al., 2010).

265

266

267 **2.4. SIMS Al-Mg isotopes analyses**

268

269 All Al-Mg isotope measurements were conducted using the IMS 1280 at the WiscSIMS  
270 Laboratory of the University of Wisconsin-Madison. The conditions for the analyses were similar  
271 to those in previous studies (Kita et al., 2012; Hertwig et al., 2019; Fukuda et al., 2020). Primary  
272 ions of  $\text{O}_2^-$  were focused in Gaussian mode with a 23 kV impact energy (-13 kV at the ion source  
273 and +10 kV at the sample surface) from the new RF ion source. Transfer optics were tuned using  
274 a Max Area of 40  $\mu\text{m}$  (magnification  $\times 200$ ). Entrance slits were set to 90  $\mu\text{m}$  and exit slits to 500  
275  $\mu\text{m}$ , which provide a MRP of  $\sim 2200$  ( $\text{M}/\Delta\text{M}$ ). Although this MRP setting is lower than that  
276 required for separating Mg hydride interferences, Hertwig et al. (2019) confirmed that  
277 interferences from hydride and  $^{48}\text{Ca}^{2+}$  are sufficiently small compared to  $\text{Mg}^+$  signals, i.e., less  
278 than 0.1‰.

279 Delta notation  $\delta^{25}\text{Mg}$  and  $\delta^{26}\text{Mg}$  used absolute Mg isotope ratios to normalize raw data as  
280 follows;  $(^{25}\text{Mg}/^{24}\text{Mg}) = 0.12663$  and  $(^{26}\text{Mg}/^{24}\text{Mg}) = 0.13932$  (Catanzaro et al., 1966). Instrumental  
281 bias was corrected using several standards matching the compositions of measured olivine,  
282 pyroxenes and plagioclase. The excess  $^{26}\text{Mg}$  after mass fractionation correction ( $\delta^{26}\text{Mg}^*$ ) was  
283 calculated using an exponential law in two steps, similarly to the approach of Hertwig et al. (2019)  
284 and as follows:

285

286 
$$\delta^{26}\text{Mg}^* = \left[ \left( 1 + \frac{\delta^{26}\text{Mg}}{1000} \right) - \left( 1 + \frac{\delta^{25}\text{Mg}}{1000} \right)^{\frac{1}{\beta}} \right] \times 1000 \quad (7)$$

287 
$$\delta^{26}\text{Mg}^* = \Delta^{26}\text{Mg} \times \left( 1 + \frac{\delta^{25}\text{Mg}}{1000} \right)^{\frac{1}{\beta}} \quad (8)$$

288

289 The exponential parameter  $\beta$  was assumed to be 0.5128 (Davis et al., 2015) for plagioclases  
 290 analyses and determined from olivine standards for olivine and pyroxene analyses. The  $\delta^{26}\text{Mg}^*$  is  
 291 equivalent to  $\Delta^{26}\text{Mg}$  when the natural mass dependent fractionation measured as  $\delta^{25}\text{Mg}$  equals  
 292 zero (Ushikubo et al., 2017). Following the procedure of Tenner et al. (2019), we assume  
 293 chondrules do not have a significant natural mass dependent fractionation in  $\delta^{25}\text{Mg}$  (~0‰) and  
 294 estimated  $\delta^{26}\text{Mg}^*$  to be the same as  $\Delta^{26}\text{Mg}$ .

295 For anorthite measurements, the relative sensitivity factors of standards were used to  
 296 correct for instrumental bias as follows:

297

298 
$$RSF = \frac{\left( \frac{^{27}\text{Al}}{^{24}\text{Mg}} \right)^{\text{SIMS}}_{\text{measured}}}{\left( \frac{^{27}\text{Al}}{^{24}\text{Mg}} \right)^{\text{EPMA}}_{\text{reference}}} \quad (9)$$

299

300 Three different analytical settings were used, two for anorthite measurements with 6  $\mu\text{m}$   
 301 and 15  $\mu\text{m}$  spot sizes, and one for olivine and pyroxenes with a 8  $\mu\text{m}$  spot size. In all sessions,  
 302 three Mg isotopes and  $^{27}\text{Al}^+$  signals were detected simultaneously on the multicollection (MC)  
 303 system. In all conditions, the major isotopes  $^{24}\text{Mg}^+$  and  $^{27}\text{Al}^+$  were detected on FCs. Minor isotopes  
 304  $^{25}\text{Mg}^+$  and  $^{26}\text{Mg}^+$  were measured on FCs for olivine/pyroxene and large spot anorthite analyses,

305 while during small spot analyses they were detected using electron multipliers (EM) on  
306 multicollector arrays (Hamamatsu EM).

307

308 *2.4.1. MC FC-EM analyses of anorthite (6  $\mu$ m spot size)*

309 Since most of the chondrules had smaller plagioclases grains (<10  $\mu$ m), two sessions were  
310 conducted using a small spot size of ~6  $\mu$ m. The primary intensity was ~160 pA, resulting in  
311 secondary  $^{24}\text{Mg}^+$  and  $^{27}\text{Al}^+$  intensities of  $(6\text{-}8)\times 10^5$  cps and  $\sim 2\times 10^7$  cps for anorthite glass standard  
312 with 1.0 wt% MgO. FC amplifier boards with  $10^{12}\ \Omega$  and  $10^{11}\ \Omega$  resistances were used for detecting  
313  $^{24}\text{Mg}^+$  and  $^{27}\text{Al}^+$ , respectively. Secondary  $^{25}\text{Mg}^+$  and  $^{26}\text{Mg}^+$  isotope signals were  $7\times 10^4$  cps to  $1\times 10^5$   
314 cps that were detected using EMs. Analyses typically consisted of 120 s of presputtering followed  
315 by centering of secondary deflectors and 400 cycles of data acquisitions with 4 s counting time.  
316 The FC baseline was measured for  $^{24}\text{Mg}^+$  during presputtering and the baseline average of 8  
317 analyses was taken as the value to correct  $^{24}\text{Mg}^+$  intensities. The variabilities of the baseline were  
318 typically ~150-180 cps (1SD). The overall analysis time was ~32 min. In order to maintain constant  
319 EM gains, relative to the FC detectors, the high voltage (HV) of each EM was adjusted at the 20<sup>th</sup>  
320 and 220<sup>th</sup> cycles using a Cameca software routine. The gain drift for each EM was monitored and  
321 corrected using a second discriminator connected parallel to the first one (Kita et al., 2019, see  
322 detailed information in EA2).

323 Two anorthite composition glass standards with MgO contents of 0.6 wt.% and 1 wt.%  
324 (Kita et al., 2012) were used to correct for RSF and  $\delta^{26}\text{Mg}^*$ , which are in the same range of MgO  
325 contents with those of the unknown plagioclase grains in the chondrules. Internal errors were  
326 typically 0.4-0.6‰ (2SE) for  $\Delta^{26}\text{Mg}$  and 0.5-1 % for  $^{27}\text{Al}/^{24}\text{Mg}$  ratios. Within several hours of  
327 continuous analyses, repeated analyses of anorthite glass standard were reproducible to nearly

328 within their internal errors. However, because of relatively high intensities applied to the EMs  
329 ( $\sim 10^5$  cps), the measured Mg isotope ratios of the standard drifted over the entire analysis sessions.  
330 The first session was corrected for a 6‰ drift of the  $\Delta^{26}\text{Mg}$  values during the entire session of five  
331 days, using a weighted least square algorithm for each day of analysis (EA3). The second session  
332 did not require any drift correction in-between mass calibrations, which represent approximately  
333 one day of analyses. As for the O isotope analyses, the p-value of each coefficient were checked  
334 to determined which was the best polynomial order to use for the drift correction. The  
335 reproducibility for standard analyses after drift correction was typically 0.4-0.7‰ (2SD) for  $\Delta^{26}\text{Mg}$ .  
336 Some analyses that touched a high-Ca pyroxene were stopped before the end of the 400 cycles.  
337 For such analyses, only the cycles before the abrupt increase of  $\text{Mg}^+$  were taken to calculate the  
338  $\Delta^{26}\text{Mg}$  and  $^{27}\text{Al}/^{24}\text{Mg}$  ratios and the standard analyses used for calibrating  $\delta^{26}\text{Mg}^*$  were also  
339 recalculated using the same number of cycles in order to account for the change in  $^{27}\text{Al}/^{24}\text{Mg}$  and  
340 a potential bias in  $\Delta^{26}\text{Mg}$  with the depth of analysis (Hertwig et al., 2019). Final uncertainties for  
341  $\delta^{26}\text{Mg}^*$  represent the propagation of internal errors (2SE), errors in the fit for the drift correction  
342 at the time of the analysis (95% confidence interval) and the 2SE of the standard measurements.  
343 This uncertainty is dominated by the internal error. The uncertainties for the  $^{27}\text{Al}/^{24}\text{Mg}$  ratios  
344 represents the propagation of internal errors (2SE) and the 2SE of the standard measurements.  
345 Again, this uncertainty is dominated by the internal error. Two brackets of standards behaved  
346 significantly differently during the middle of the second session (red section in EA3, spreadsheet  
347 “07-23-2019”).  
348  
349 2.4.2. *MCFC analyses of anorthite (15  $\mu\text{m}$  spot size)*

350 An O<sub>2</sub><sup>-</sup> primary intensity of 4 nA resulted in secondary <sup>24</sup>Mg<sup>+</sup> and <sup>27</sup>Al<sup>+</sup> intensities of  
351 ~2×10<sup>7</sup> cps and ~5×10<sup>8</sup> cps for the anorthite glass standard with 1.0 wt% MgO. FC detectors were  
352 used for all three Mg isotope signals with 10<sup>12</sup> Ω resistances and <sup>27</sup>Al<sup>+</sup> with 10<sup>11</sup> Ω resistance. The  
353 analyses consisted of 100 sec of presputtering, followed by the alignment of secondary deflectors  
354 and 20 cycles of data acquisitions with 10 s counting time for each cycle. The overall analysis time  
355 was ~8 min. As in the FC-EM sessions, two glass standards (0.6 wt.% and 1 wt.% of MgO) were  
356 used to correct for instrumental bias. For Δ<sup>26</sup>Mg, internal errors were typically 0.2-0.45‰ (2SE),  
357 and the reproducibility for the 34 standard measurements of the session was 0.38‰ (2SD). A slight  
358 linear drift correction was required for the entire session that lasted ~6h because we started the  
359 analyses within several hours of switching the FC amplifier boards. The <sup>27</sup>Al/<sup>24</sup>Mg ratios had  
360 internal errors of 0.15-0.2% and a reproducibility for the 34 standard measurements of 0.25%  
361 (2SD). The errors in the <sup>27</sup>Al/<sup>24</sup>Mg ratios were propagated the same way as for FC-EM data.

362

#### 363 2.4.3. MCFC analyses of olivine and pyroxenes (8 μm spot size)

364 A 1 nA O<sub>2</sub><sup>-</sup> focused primary beam resulted in the secondary <sup>24</sup>Mg<sup>+</sup> intensity of ~2×10<sup>8</sup> cps  
365 for olivine and pyroxene that was measured with a FC detector with a 10<sup>10</sup> Ω resistor. The masses  
366 <sup>25</sup>Mg<sup>+</sup>, <sup>26</sup>Mg<sup>+</sup> and <sup>27</sup>Al<sup>+</sup> were measured using FC detectors with 10<sup>11</sup> Ω resistors. Counting times  
367 were the same as for the MCFC analyses of anorthite. Fifteen different olivine standards (Fo<sub>60</sub>-  
368 Fo<sub>100</sub>) and five pyroxene standards (two diopside and three low-Ca pyroxenes with Mg# 85-96  
369 mole%) were measured to correct for natural and instrumental bias (Fukuda et al., 2020). With  
370 such a large number of standards the exponential factor β was determined using olivine standards  
371 by fitting the data in a δ<sup>26</sup>Mg' vs δ<sup>25</sup>Mg' diagram, with δ<sup>26-25</sup>Mg' = 1000 × ln { (δ<sup>26-25</sup>Mg + 1000) /  
372 1000 }, resulting in a nominal value of 0.5169 (EA3 spreadsheet “d25Mg vs d26Mg” and EA4).

373 This nominal value was obtained using only terrestrial olivine standards since extraterrestrial  
374 olivine standard might have very small variabilities in  $\Delta^{26}\text{Mg}$ . Olivine  $\Delta^{26}\text{Mg}$  values exhibited a  
375 small offset of  $0.019 \pm 0.010\text{\textperthousand}$  (2SE) and pyroxene  $\Delta^{26}\text{Mg}$  values were higher by  $0.15 \pm 0.025\text{\textperthousand}$   
376 (2SE) relative to the San Carlos olivine (SC-Ol) standard (EA4). Such offset between olivine and  
377 pyroxene might be due to small degree of mass independent fractionation within the SIMS  
378 instrument, which seem to occur in our analyses using finely focused intense primary beam  
379 conditions. This would not be fully evaluated in previous studies which used a smaller number of  
380 olivine and low-Ca pyroxene standards (typically only 2 for each in contrast to 15 olivine and 5  
381 pyroxene standards in this study), but include several glass standards to estimate instrumental  
382 fractionation law.

383 Since terrestrial olivine does not exhibit any natural excess  $^{26}\text{Mg}$ , no additional correction  
384 was required for these standards. Standards of meteoritic origin were corrected by their known  
385  $\delta^{26}\text{Mg}^*$ , i.e.  $0.0082 \pm 0.0011\text{\textperthousand}$  for KN-Ol (Kenna olivine; Larsen et al., 2011),  $0.0085 \pm 0.0018\text{\textperthousand}$   
386 for SW-Ol (Springwater olivine; Larsen et al., 2016). The natural excess  $^{26}\text{Mg}$  of one meteoritic  
387 olivine standard was unknown (WN-Ol, Winona olivine), and was not used to correct the  $\Delta^{26}\text{Mg}$   
388 values. Additionally, the most Fe-rich standard (Fo<sub>59</sub>) was not used since it was well below the Fo  
389 range of olivine unknowns of this study.  $\Delta^{26}\text{Mg}$  values during the session were corrected for drift  
390 by dividing it into three sections in which simple linear corrections were possible. Internal errors  
391 for  $\Delta^{26}\text{Mg}$  were typically 0.04-0.07% for the olivine measurements, and slightly higher for the  
392 pyroxene analyses at 0.06-0.15% (2SE). The reproducibility of the standard measurements after  
393 drift correction was typically 0.04-0.06% (2SD) for SC-Ol standard. The error propagation was  
394 the same as used for anorthite measurements.

395

396 2.4.4 *Isochron regression*

397 Isochron regressions were computed using the online version of IsoplotR (Vermeesch,  
398 2018) with the maximum likelihood option, i.e., Model 1 (York et al., 2004). Uncertainties on  
399  $^{27}\text{Al}/^{24}\text{Mg}$  used for the regression did not take into account the uncertainty on the reference value  
400 (from EPMA measurements) for anorthite standards. Since uncertainty of the slopes are larger than  
401 1% for all studied chondrules, it would not change the final uncertainty of the isochron slopes.  
402 Weighted means were also computed using the IsoplotR software.

403

404

405 **3. RESULTS**

406

407 Fourteen chondrules from five different chondrites were investigated for O and Al-Mg  
408 isotopes in this study. Among them, four chondrules are from QUE 97008, four from NWA 8276,  
409 two from NWA 8649, two from Semarkona and two from MET 00452. Oxygen three isotopes, as  
410 well as Al-Mg isotopes, were obtained for all chondrules. One chondrule from Semarkona (c34)  
411 had been previously analyzed for Al-Mg isotopes and O three isotopes (CH23 in Kita et al., 2000  
412 and Kita et al., 2010, respectively). Nevertheless, due to the improved precision for both methods,  
413 it was analyzed with all other chondrules, except for the EPMA measurements of silicate minerals.

414 Full analyses for all phases are accessible in the supplementary materials. The EPMA  
415 analyses of olivine, pyroxenes and plagioclases are located in EA5. SIMS O isotopes data are in  
416 EA1 and Al-Mg isotopes analyses are in EA3. Pictures for all SIMS pits for both methods, as well  
417 as BSE images of the locations of these analyses inside each chondrule are provided in EA6.

418

419 **3.1 Petrography of chondrules and mineral chemistry**

420

421 Figs. 1 and 2 show all chondrules analyzed for Al-Mg and O isotopes. Tables 1, 2 and 3  
422 list the olivine, pyroxene and plagioclase compositions, respectively. The petrography and mineral  
423 chemistry of these chondrules are described below. Three out of the 14 selected chondrules were  
424 FeO-poor ( $Mg\# > 90$ ), while the others are FeO-rich ( $Mg\# < 90$ ) with a wide range of  $Mg\#$  (76-90).  
425 Typical porphyritic chondrules are subdivided into types I and II according to  $Mg\# > 90$  and  $< 90$ ,  
426 respectively, and into porphyritic olivine (PO), porphyritic olivine pyroxene (POP), and  
427 porphyritic pyroxene (PP) chondrules according to the modes of olivine and pyroxene phenocrysts;  
428 olivine volume %  $> 80\%$ ,  $20\text{-}80\%$ ,  $< 20\%$ , respectively, (Jones, 1994). Here, we adopt these  
429 classification schemes to anorthite-bearing chondrules studied here.

430

431 *3.1.1. Type I plagioclase-bearing chondrules*

432 Two type-I POP chondrules, NWA 8276 c69 (Fig. 1a) and QUE 97008 c61 (Fig. 1b), show  
433 very similar textures and compositions for their olivine and pyroxene phenocrysts. Olivine  
434 phenocrysts are equant and have sizes ranging from 50-200  $\mu\text{m}$  with homogenous compositions  
435 ( $Fo_{95\text{-}97}$ , see Table 1). There are no low-Ca pyroxenes, but the pyroxenes that are present have  
436 limited amounts of Ca with compositions of ( $Wo_7En_{90}Fs_3$  for NWA8276 c69) and ( $Wo_{13}En_{80}Fs_7$   
437 for QUE97008 c61), respectively (Table 2). These pyroxenes are interstitial to the larger olivine  
438 phenocrysts. The remaining space is occupied by interstitial plagioclase grains with  $An_{99}$  in both  
439 chondrules (Table 3). Another type I chondrule is a PP chondrule, NWA 8649 c17 (Fig. 1c), which  
440 exhibits an inverse zoning in its pyroxene phenocrysts, with increase of  $Mg\#$  toward the rims, from  
441  $Wo_3En_{85}Fs_{12}$  in the core to  $Wo_3En_{90}Fs_7$  at the rims (see EA5). The boundaries between cores and

442 rims are very sharp. Small high-Ca pyroxene overgrowths can be observed. Plagioclase is present  
443 as an interstitial phase with a composition of  $\sim\text{An}_{94}$ .

444

445 *3.1.2. Type II plagioclase-bearing chondrules*

446 Four type II chondrules can be grouped together by their similar textures, which include  
447 NWA 8276 c7 (Fig. 1d), QUE 97008 c51 (Fig. 1e) and c143 (Fig. 1f) and NWA 8649 c87 (Fig.  
448 2a). These chondrules can all be classified as type II-PO and have large olivine phenocrysts with  
449 only minor amounts of interstitial low-Ca pyroxenes that exhibit zoning toward more pigeonitic  
450 compositions, except for NWA 8276 c7 that does not have any low-Ca pyroxene. Plagioclase  
451 occurs as elongated laths, except for NWA 8649 c87 where the plagioclase grains are interstitial  
452 and not euhedral. Their Fo contents range between Fo<sub>85</sub> and Fo<sub>90</sub> (Table 1), while the Mg# of  
453 pyroxene phenocrysts are between 81 and 91 with low Ca content, Wo<sub>4-5</sub>, except for NWA 8276  
454 c7 with up to Wo<sub>11</sub> (Table 2).

455 MET 00452 c19 is a very large type II-PO chondrule (2.5-3 mm) with barred olivine  
456 phenocrysts (Fig. 2b). The olivine phenocrysts are elongated in one direction and show a slight  
457 zonation toward the rims as can be seen in a BSE image (Fig. 2b). The cores of the olivine  
458 phenocrysts have compositions of Fo<sub>83</sub> with a limited zoning toward the rims, which did not allow  
459 us to obtain a good EPMA measurement of the Fe-rich rim with a 3 $\mu\text{m}$  spot size. The plagioclase  
460 grains are elongated at a high angle to the olivine orientation, with a 60° angle. The pyroxene  
461 grains (Wo<sub>3</sub>En<sub>86</sub>Fs<sub>11</sub>) are interstitial to the plagioclase grains and the olivine phenocrysts. The  
462 plagioclase grains have a composition of  $\sim\text{An}_{98}$ .

463 MET 00452 c111 is a type II-POP chondrule (Fig. 2c). The olivine phenocrysts are large  
464 and euhedral with a homogeneous composition of  $\sim\text{Fo}_{90}$ . Subordinate pyroxene grains

465 (Wo<sub>3</sub>En<sub>89</sub>Fs<sub>8</sub>) occur between the larger olivine phenocrysts. The plagioclase grains, which are  
466 interstitial to the pyroxene grains and the olivine phenocrysts, have a composition of ~An<sub>98</sub>.

467 NWA 8276 c87 (Fig. 2d) is a large (~800  $\mu\text{m}$ ) type II-POP chondrule, in which olivine  
468 phenocrysts are small and homogeneously distributed. The olivine core compositions are ~Fo<sub>83</sub>  
469 with zoning toward the rims. The pyroxene grains are very small and occur along the rims of the  
470 olivine phenocrysts. The plagioclase occurs as euhedral, elongated grains with a composition of  
471 ~An<sub>97</sub>.

472 QUE 97008 c150 (Fig. 2e) is mainly composed of large olivine phenocrysts with small  
473 low-Ca pyroxene in between and interstitial plagioclase grains. The olivine phenocrysts are  
474 homogeneous (~Fo<sub>77</sub>). The low-Ca pyroxene grains are interstitial between the olivine phenocrysts  
475 with a composition of Wo<sub>3</sub>En<sub>89</sub>Fs<sub>8</sub>. The plagioclase grains have a composition of ~An<sub>97</sub>. One  
476 olivine phenocrysts on the edge of the chondrule (upper left corner in Fig. 2e) shows complex  
477 zoning with a core of ~Fo<sub>95</sub>, then a diffuse zonation toward ~Fo<sub>97</sub>, surrounded by olivine that  
478 approaches the composition of the other olivine grains (~Fo<sub>80</sub>) in this chondrule.

479 Semarkona c47 (Fig. 2f) is a large chondrule (~1.5 mm) mainly composed of small olivine  
480 phenocrysts. The olivine phenocrysts are homogeneous (~Fo<sub>86</sub>) and have small overgrowths of  
481 high-Ca pyroxene that were too small to be accurately analyzed (i.e., below a few  $\mu\text{m}$ ). The  
482 plagioclase grains are interstitial to the pyroxene grains and the olivine phenocrysts and have  
483 nearly endmember anorthite composition (~An<sub>100</sub>).

484 NWA 8276 c88 is clearly mineralogically zoned, with only anorthite grains, small high-Ca  
485 pyroxene grains and euhedral FeO-rich olivine phenocrysts in its core (Fig. 2g). The low-Ca  
486 pyroxene grains are only located in the rim of the chondrule, with abundant rounded inclusions of  
487 olivine (i.e., named chadacrysts in Jones, 1989) and have composition of Wo<sub>1</sub>En<sub>83</sub>Fs<sub>16</sub>. The Fo

488 contents of the olivine chadacrysts in the low-Ca pyroxene grains are higher (~Fo<sub>80</sub>) than the Fo  
489 contents of the euhedral olivine phenocrysts in the core of the chondrule (~Fo<sub>77</sub>). Additionally,  
490 some zoning can be observed in the low-Ca pyroxenes at the boundary between the core and rim  
491 of the chondrule, with slightly lower Mg# (~75 mole%) and higher Ca content in the core than in  
492 the rim (Mg# ~84 mole%). Plagioclase compositions are nearly pure anorthite with An<sub>99</sub>.

493 Semarkona c34 (formally named as CH23 in Kita et al., 2000; 2010; Tachibana et al., 2003)  
494 is also mineralogically zoned with large olivine phenocrysts in the center of the chondrule, while  
495 low-Ca pyroxene grains are only located in the rim of the chondrule, with rounded inclusions of  
496 olivine grains (Fig. 2h). Kita et al. (2000) determined the olivine chadacrysts to have Mg# of 82  
497 mole% and the low-Ca pyroxene to have a composition of Wo<sub>2-5</sub>En<sub>76-82</sub>Fs<sub>16-19</sub>. The plagioclase  
498 compositions are nearly pure anorthite with An<sub>100</sub>.

499 A good example of the distribution of O and Al-Mg isotopes analyses is illustrated for the  
500 Semarkona c34 chondrule in Fig. 3.

501

### 502 *3.1.2. Mineral Chemistry*

503 The Mg# of olivine and pyroxene range from 77 to 97. In most chondrules, both olivine  
504 and pyroxenes are homogeneous in Mg#, with internal variations less than 1% (1SD). Fo content  
505 of olivine and En content of low-Ca pyroxene are usually in agreement within  $\pm 2$  mole%, even  
506 for NWA 8649 c17 where only pyroxene analyses were taken from the rims. Olivine grains of all  
507 chondrules have Mn compositions that lie between type II-PO chondrule olivine grains from  
508 ordinary chondrites (OC line, Fig. 4a) and CO chondrites (CO line, Fig. 4a) (Berlin et al., 2011).  
509 The Cr<sub>2</sub>O<sub>3</sub> contents of ferroan olivine core for all chondrules are between 0.2-0.8 wt% and exhibit

510 a slight decrease with increasing FeO contents (Fig. 4b), typical for olivine grains of chondrules  
511 from UOCs of low subtypes 3.00-3.05 (Grossman and Brearley, 2005).

512 Some chondrules have euhedral plagioclases, usually euhedral elongated grains (NWA  
513 8276 c7, c87, c88; MET 00452 c19; Semarkona c34; QUE 97008 c51, c143, c150), whereas others  
514 have more interstitial shaped grains with habitus delineated by the surrounding mineral grains  
515 (NWA 8276 c69; MET 00452 c111; Semarkona c47; QUE 97008 c61; NWA 8649 c17 and c87).

516 No zonation is observed at the rim of anorthite grains for all studied chondrules. The plagioclases  
517 selected for this study are mostly pure anorthite ( $An > 95\%$ ), with only two chondrules from NWA  
518 8649 (c17 and c87) that have plagioclase compositions of  $\sim An_{93}$  and  $\sim An_{94}$ , respectively. The  
519 measured plagioclase compositions in this study is only 85-91 mole %  $CaAl_2Si_2O_8$  due to both the  
520 incorporation of Fe and Mg and because the  $NaAlSi_3O_8$  endmember only account for 0.2-6.0  
521 mole%. They have extremely low  $KAlSi_3O_8$  concentrations, usually well below 1%. Silica excess  
522 is found in all chondrules except both chondrules from NWA 8649. There is a correlation between  
523 An content and silica excess (Fig. 5a) although the small range of An composition for these  
524 plagioclases grains precludes any robust interpretation. Their MgO contents are mostly between  
525 0.5 and 1 wt%, with only 3 analyses higher than 1 wt% (Fig. 5b). The Mg and Fe contents of  
526 plagioclases are clearly related to the substitution (5) for all chondrules with  $Ca(Mg,Fe,Mn)Si_3O_8$   
527 end-members between 3 and 8 mole%.  $(Mg,Fe,Mn)Al_2Si_2O_8$  end-member only account for a minor  
528 amount of Mg and Fe incorporation with end-members between 0.8 and 2.6 mole%.

529

### 530 **3.2 Oxygen three-isotopes**

531

532 Table 4 shows the mean values for  $\delta^{18}\text{O}$ ,  $\delta^{17}\text{O}$  and  $\Delta^{17}\text{O}$  for all chondrules studied in this  
533 paper. Among the 14 chondrules, NWA 8276 c69 exhibits large variations in both  $\delta^{18}\text{O}$  and  $\delta^{17}\text{O}$   
534 after the instrumental bias correction, which are likely related to a large hole in the sample surface  
535 near the chondrule. The SIMS secondary ion deflector (DTFA-XY) adjustments exceeded their  
536 normal range ( $\pm 50$  bits) for this chondrule, which is known to create larger analytical fractionation  
537 for O isotopes (Kita et al., 2009). Therefore, we decided not to include  $\delta^{18}\text{O}$  and  $\delta^{17}\text{O}$  values of  
538 this chondrule in the final reported values. Nevertheless, instrumental fractionations on  $\delta^{18}\text{O}$  and  
539  $\delta^{17}\text{O}$  are mass-dependent, so that the  $\Delta^{17}\text{O}$  values are not affected and reported in the Table 4.  
540 Except for NWA 8276 c69, individual SIMS spot analyses of each chondrule are shown in Fig. 6  
541 and Fig. 7.

542 Half of the chondrules studied here show a small variation in  $\delta^{18}\text{O}$  and  $\delta^{17}\text{O}$  beyond their  
543 analytical uncertainties. Seven chondrules have internally homogeneous olivine and pyroxene  
544 isotope ratios throughout the entire chondrule, i.e., QUE 97008 c51 (Fig. 6a), NWA 8276 c87 (Fig.  
545 6b), Semarkona c47 (Fig. 6c), c34 (Fig. 6d), MET 00452 c19 (Fig. 6e), c111 (Fig. 6f) and NWA  
546 8649 c17 (Fig. 7g). In contrast, some O isotope data for individual chondrules shows a clear spread  
547 along a 1:1 line, such as NWA 8276 c7 (Fig. 7a) and NWA 8276 c88 (Fig. 7b), while others show  
548 mass dependent fractionation (slope = 0.52), such as QUE 97008 c61 (Fig. 7c), c143 (Fig. 7d),  
549 c150 (Fig. 7e), NWA 8649 c87 (Fig. 7f). The data excluded from the computation of the host  
550 chondrule values are displayed as slightly transparent in Figs. 6 and 7. One chondrule contained  
551 what seems to be a relict olivine at its edge (QUE 97008 c150, Fig. 2d), that exhibits Fe-Mg zoning  
552 and has significantly different O isotope ratios compared to the rest of analyses in this chondrule.  
553 Interestingly, the analyses of the core of the relict olivine grain gave only slightly lower values  
554 ( $\delta^{18}\text{O} = 3.86 \pm 0.26\text{\textperthousand}$ ,  $\delta^{17}\text{O} = 1.85 \pm 0.20\text{\textperthousand}$ ) than the rest of the analyses ( $\delta^{18}\text{O} = 4.54 \pm 0.40\text{\textperthousand}$ ,

555  $\delta^{17}\text{O} = 2.34 \pm 0.42\text{\textperthousand}$ ), see EA1. On the other hand, an analysis from the rim of this grain gave very  
556 different results than the rest of the olivine analyses ( $\delta^{18}\text{O} = 5.44 \pm 0.26\text{\textperthousand}$ ,  $\delta^{17}\text{O} = 3.86 \pm 0.20$ ).  
557 Both analyses were removed from the computation of the mean for this chondrule.

558 The host chondrule  $\delta^{18}\text{O}$  values range from  $3.45 \pm 0.36\text{\textperthousand}$  (2SE) to  $5.64 \pm 0.47\text{\textperthousand}$  (2SE).  
559 The  $\delta^{17}\text{O}$  values range from  $1.36 \pm 0.32\text{\textperthousand}$  to  $3.29 \pm 0.29\text{\textperthousand}$ . The  $\Delta^{17}\text{O}$  values range from  $-0.44 \pm$   
560  $0.23\text{\textperthousand}$  to  $0.49 \pm 0.15\text{\textperthousand}$  with the mean value of  $0.05 \pm 0.51\text{\textperthousand}$  (2SD, n=14). The host chondrule  
561 data fall on a steeper slope than the terrestrial mass fractional line (slope = 0.52), with an  
562 approximate slope of 1 (Fig. 8a). They all fall between the Equilibrated Chondrite Line (ECL,  
563 Clayton et al., 1991) and the Primitive Chondrule Minerals line (PCM, Ushikubo et al., 2012).  
564 Overall, the chondrules have O three isotope compositions that are in good agreement with the  
565 plagioclase-bearing chondrules of UOCs from Kita et al. (2010) and tend to show at the lowest  
566 end of  $\Delta^{17}\text{O}$  distributions among LL3 chondrules (mean value of  $0.5 \pm 0.9\text{\textperthousand}$ , 2SD, n=33).  
567 Chondrules within a single chondrite form clusters of data (Fig. 8a), except for NWA 8276 in  
568 which c87 is at the lower end of the cloud of values whereas the two other chondrules are at the  
569 higher end. No correlation between Mg# and O three isotopes was found (Fig. 8b).

570 Additionally, two analyses of plagioclase were obtained in two chondrules NWA 8276 c7  
571 and c88, where the plagioclase grains were big enough to measure with 12  $\mu\text{m}$  spots. The  
572 plagioclase analyses in NWA 8276 c7 (Fig. 7a) are slightly deviated to higher  $\delta^{17}\text{O}$  and  $\delta^{18}\text{O}$   
573 compared to those of the olivine and pyroxene analyses, though data from plagioclase in c88  
574 overlaps with the olivine and pyroxene analyses in the same chondrule (Fig. 7b). In both cases, the  
575 differences between the plagioclase and the host chondrules are less than 1 $\text{\textperthousand}$ , which is much  
576 smaller than is the case for glassy mesostasis in LL3.0-3.1 chondrules (as high as  $\sim 10\text{\textperthousand}$ ; Kita et  
577 al., 2010).

578

579 **3.2 Al-Mg systematics**

580

581        Between 8 to 18 analyses were done in each chondrule (Table 5). In each chondrule, four  
582 analyses of pyroxene and/or olivine grains were measured. In Semarkona c34, four MCFC  
583 analyses were possible in anorthite grains, in NWA 8276 c69 only three MCFC points were  
584 measured and, finally, in NWA 8276 c88, five MCFC points were determined. Since all  
585 plagioclase grains analyzed during this study are very close to pure anorthite in composition and  
586 has between 0.5-1 wt.% MgO, the  $^{27}\text{Al}/^{24}\text{Mg}$  ratios are all between 33 and 76. Usually, the Al-Mg  
587 isochrons are drawn through two clusters of points, pyroxenes/olivines near the origin and  
588 plagioclases for high Al/Mg ratios. In this case, most of the chondrules exhibit some variations for  
589 the plagioclases measured, with the  $^{27}\text{Al}/^{24}\text{Mg}$  ratios typically vary by 10-15. Some chondrules  
590 show even larger spreads in Al/Mg ratios in plagioclases such as NWA 8276 c88 from 45 to 76 or  
591 MET 00452 c111 from 41 to 66. On the other hand, some chondrules have plagioclase  $^{27}\text{Al}/^{24}\text{Mg}$   
592 ratios that show small variabilities  $\leq 10$ , such as QUE 97008 c61 and c150, NWA 8649 c17, NWA  
593 8649 c87, Semarkona c47, or NWA 8276 c69. All analyses of plagioclases exhibit resolvable  
594 excesses in  $^{26}\text{Mg}$ , which range between  $1.0 \pm 0.4\text{\textperthousand}$  and  $4.8 \pm 0.6\text{\textperthousand}$ . The  $^{27}\text{Al}/^{24}\text{Mg}$  ratios of  
595 pyroxene grains are generally higher (from 0.003 to 0.08) than olivine grains ( $1 \times 10^{-4}$  to  $7 \times 10^{-3}$ ).  
596 The  $\delta^{26}\text{Mg}^*$  values of the olivines and pyroxenes are all within uncertainty of the measurements,  
597  $\pm 0.10\text{\textperthousand}$ . The Al-Mg isochron regressions of individual chondrules are well-behaved, with MSWD  
598 between 0.37 and 1.8, except for one chondrule NWA 8649 c87 that will be discussed later. These  
599 values are very significant since the degrees of freedom range between 6 and 14, and higher  
600 degrees of freedom require MSWD that are closer to 1 to be considered as isochrons (Wendt and

601 Carl, 1991). The  $(^{26}\text{Al}/^{27}\text{Al})_0$  of the chondrules range from  $(6.3 \pm 0.4) \times 10^{-6}$  to  $(8.9 \pm 0.2) \times 10^{-6}$   
602 (Table 5). The inferred  $(^{26}\text{Al}/^{27}\text{Al})_0$  of chondrules are converted into relative crystallization ages  
603 after CAIs using the canonical value of  $5.25 \times 10^{-5}$  (Jacobsen et al., 2008; Larsen et al., 2011) under  
604 the assumption of a homogeneous distribution of  $^{26}\text{Al}$  in the early Solar System (Kita et al., 2013;  
605 Budde et al., 2018). The range of ages from these chondrules is between  $1.80 \pm 0.04$  Ma to  $2.16 \pm$   
606  $0.11$  Ma after CAIs. The intercepts of all regressions  $(\delta^{26}\text{Mg}^*)_0$  range between  $-0.043 \pm 0.046\%$   
607 (2SD) and  $+0.046 \pm 0.046\%$  (2SD). They all are indistinguishable from 0 within errors. Ages  
608 obtained for the two chondrules using both MCFC and FC-EM methods are similar within errors  
609 (Semarkona c34 and NWA 8276 c88, see Table 5). The errors for age represent 95% confidence  
610 interval, they range from 0.04 Ma to 0.16 Ma.

611 Of the 14 chondrules analyzed, only one chondrule NWA 8649 c87 resulted in an  
612 errorchron with a MSWD of 4.7 when taking all analyses. However, only one point was  
613 significantly lower than the rest (PI #2 in EA3). When comparing the SE and BSE images of SIMS  
614 spots for all anorthite analyses, no clear evidence was found to reject this analysis. We choose to  
615 remove this point from the fit and it results in a MSWD of 2.1, within acceptable bound for this  
616 degree of freedom. Isochron diagrams of QUE 97008 c143 and c150, MET 00452 c111, and NWA  
617 8276 c69 also show small scatter from regression lines, which are not as significant as NWA 8649  
618 c87. Their MSWD are from 1.2 to 1.8, which are acceptable ranges.

619 It is evident that chondrules in QUE 97008 have a younger age than the chondrules from  
620 the other chondrites, except NWA 8276 c69. Some chondrules from the same meteorite yield ages  
621 that are resolved from each other. For example, NWA 8276 c69 ( $2.04 \pm 0.07$  Ma) is younger than  
622 the other chondrules in the same meteorite (mean age of  $1.86 \pm 0.10$  Ma). Similarly, chondrules in  
623 QUE 97008 seems to have two population of ages, with chondrules c51 and c61 at  $2.00 \pm 0.04$  Ma

624 and  $2.00 \pm 0.06$  Ma, respectively, compared to chondrules c143 and c150 that have ages of  $2.16 \pm$   
625  $0.06$  Ma and  $2.13 \pm 0.07$  Ma, respectively. We also note that some of these chondrules are those  
626 with slightly scattered data on the isochron diagrams. Interestingly, both QUE 97008 and NWA  
627 8276 are L chondrites. Indeed, all ages younger than 1.95 Ma are found in these two chondrites.  
628 L(LL) and LL chondrites only have chondrules with ages comprised between  $1.80 \pm 0.04$  Ma and  
629  $1.94 \pm 0.08$  Ma. Since the differences in the  $\Delta^{17}\text{O}$  values of these chondrules types are smaller than  
630 the uncertainty of the SIMS analyses (e.g., Fig. 8b), no correlation between Al-Mg ages and  $\Delta^{17}\text{O}$   
631 values is found.

632

#### 633 4. DISCUSSION

634

##### 635 4.1 Igneous fragment vs chondrule origin

636

637 The first description of anorthite-bearing UOC chondrules was in Hutcheon and  
638 Hutchinson (1989), which they called “clast chondrule”. They obtained a well-defined Al-Mg  
639 isochron with an initial  $^{26}\text{Al}/^{27}\text{Al}$  ratio of  $(7.7 \pm 2.1) \times 10^{-6}$ , which translated to the age of  $1.95 \pm 0.29$   
640 Ma after CAIs. The object they studied had an irregular shape and minerals at its edge were  
641 terminated abruptly against the chondrule border. Additionally, the bulk composition showed the  
642 absence of volatiles with a very low Na/Al ratio and the REE patterns in the pyroxene and  
643 plagioclase were fractionated. Based on these observations, they concluded that it represents a  
644 fragment of an igneous rock. Even if the chondrules studied in this paper resembled the object  
645 described by Hutcheon and Hutchinson (1989), several aspects challenge their interpretation. First,  
646 most of the chondrules presented here are rounded and do not seem to represent fragments of

either chondrules or igneous clasts. Second, the Mg# of both olivine and pyroxene grains span a wide range of compositions (from  $76.6 \pm 0.7$  to  $97.1 \pm 0.4$ ), which makes it hard to explain them as the products of igneous crystallization in a single asteroidal body. At least one chondrule exhibits clear mineralogical zoning (NWA 8276 c88, Fig. 2g), with low-Ca pyroxene in the rim with rounded inclusion of olivine ( $\text{Fo}_{80.6 \pm 0.7}$ ) and euhedral grains of olivine ( $\text{Fo}_{76.6 \pm 0.7}$ ) and anorthite in the core. Additionally, pyroxenes exhibit a diffuse zoning at the boundary between rim and core (see EA6 c88 image A), with higher FeO contents in the core. The mineral zoning from rim to core and the texture of the core indicate that a sequence of crystallization started from the outer rim to the inner core. Thus, they represent chondrules that were heated at high temperatures and cooled from their peripheries, rather than fragments of igneous objects. Additionally, the  $\Delta^{17}\text{O}$  values are slightly variable among anorthite bearing chondrules, which argue against their origin from a single igneous object. The O isotopes signatures for these chondrules overlaps significantly to other chondrules from UOCs (Kita et al., 2010), suggesting a common formation regions for these anorthite-bearing chondrules and typical UOCs chondrules.

Even though the studied chondrules do not represent the most common type of chondrules in ordinary chondrites, they have been widely used for Al-Mg chronology (Kita et al., 2000; Mostefaoui et al., 2002; Tachibana et al., 2003). Several large chondrules studied for both Pb-Pb and Al-Mg age determinations by Bolland et al. (2019) seem to contain anorthite-rich plagioclase. Tachibana et al. (2003) obtained a bulk chondrule composition for one of the chondrules studied here (Semarkona c34) and compared its major element composition to other, more typical, type-II chondrules. It seems to have more refractory elements (Ca and Al) and less volatiles elements (Na and Mn) than other type-II chondrules from Semarkona. This is in agreement with the observation of lower Mn content in olivine (Fig. 4a) and the very high An content of plagioclases. Since Mn

670 condenses more at higher temperature than Na in dust-enrich system (e.g., 100 $\times$  Solar composition  
671 gas; Ebel and Grossman, 2000), the very low Na/Ca ratios of these chondrules could be explained  
672 by heating at temperatures lower than condensation of Mn, where Na would have been evaporated.  
673 Alternatively, these chondrules could have formed from Na and Mn depleted precursors that were  
674 enriched in refractory elements. Either cases, these chondrules are different from typical UOC  
675 chondrules, in which the partitioning of Na between olivine and glass shows little evidence for Na  
676 evaporation indicative of a high dust density (10 $^6$  $\times$  Solar composition gas) in the local disk  
677 environments that could have prevent evaporation of Na (Alexander et al., 2008).

678

#### 679 **4.2. Minimal secondary effects on Al-Mg system**

680

681 Several observations points toward the fact that the extent of parent-body metamorphism  
682 has not significantly modified the Al-Mg system of the studied chondrules. First, we have selected  
683 a suite of least metamorphosed UOCs (3.00-3.05) based on the Cr<sub>2</sub>O<sub>3</sub> contents in olivine  
684 (Grossmann and Brearley, 2005), as also shown from olivine analyses of individual chondrules  
685 with consistently high Cr<sub>2</sub>O<sub>3</sub> contents (Fig. 4b). Second, the presence of excess silica in  
686 plagioclases in almost all chondrules, except the two chondrules from NWA 8649, are at similar  
687 levels to the primitive Acfer 094 (ungrouped C3.00) and CR chondrites, which experienced  
688 minimal thermal metamorphism (Tenner et al., 2019). Third, the well-behaved <sup>26</sup>Al-<sup>26</sup>Mg isochron  
689 (MSWD~1) for most chondrules (Figs. 9-10). Particularly, excess silica has been shown to occur  
690 only in very high temperature plagioclase, i.e., 1100-1500 °C (Longhi and Hays, 1979). Any  
691 subsequent parent body metamorphism and/or aqueous alterations would have resulted in the  
692 elimination of the excess silica content, incorporation of alkali elements, as well as formation of

secondary phases such as nepheline, sodalite, and clay minerals, which are not observed from chondrules in this study. Van Orman et al. (2014) discussed the time required for modifying Al-Mg ages in plagioclase as a function of grain sizes and self-diffusion coefficient at given temperatures and plagioclase compositions. According to the results given by Van Orman et al. (2014), the  $^{26}\text{Al}$ - $^{26}\text{Mg}$  age would be reset by 0.7 Ma (one half-life, i.e., 50% loss of excess  $^{26}\text{Mg}$ ) in a 20  $\mu\text{m}$  spherical anorthite grain (10  $\mu\text{m}$  radius) by 0.56 Ma at 500  $^{\circ}\text{C}$  and 1363 Ga at 300  $^{\circ}\text{C}$ . Since Semarkona is known to have never experienced parent body temperatures higher than 260  $^{\circ}\text{C}$  (Alexander et al., 1989), resetting the two Semarkona chondrules studied here is impossible. All chondrites selected for this work are low subtype UOCs (3.00-3.05), they most probably never experienced temperature above 500  $^{\circ}\text{C}$  (Kimura et al., 2008) and resetting their  $^{26}\text{Al}$ - $^{26}\text{Mg}$  age by one half-life would take several millions of years for the biggest plagioclase grains. Since all ages exhibit a restricted range, and that at least the Semarkona chondrules and the biggest plagioclase grains cannot realistically be reset by Mg diffusion, it is very unlikely that the majority of Al-Mg isotope systematics presented in this study have been reset during parent body metamorphism.

707

### 708 **4.3 Timing of anorthite-bearing chondrule formation**

709

710 Fig. 11 show the range of  $(^{26}\text{Al}/^{27}\text{Al})_0$  of the chondrules, from  $(6.3 \pm 0.7) \times 10^{-6}$  to  $(8.9 \pm 0.3) \times 10^{-6}$ . This corresponds to a range of ages comprised between  $1.80 \pm 0.04$  Ma to  $2.16 \pm 0.11$  Ma after CAIs. The kernel distribution shows a major peak at  $\sim 1.9$  Ma that extend to 2.2 Ma (Fig. 11b). The range is consistent with anorthite-bearing chondrule data from L/LL 3.00-3.15 chondrites with inferred  $(^{26}\text{Al}/^{27}\text{Al})_0$  of  $7 \times 10^{-6}$  to  $1.0 \times 10^{-5}$  with uncertainties typically from  $(1-5) \times 10^{-6}$  (Hutcheon and Hutchison, 1989; Kita et al., 2000, revision by Kita et al. 2010; Mostefaoui et al. 2002; Mostefoui et al., 2002; Rudraswami et al., 2007; Bollard et al., 2019). Only 2 out of

717 11 chondrules are outside of the range observed in this study; QUE 97008 (L3.05) CH#1B with  
718  $(1.95\pm0.76)\times10^{-5}$  (Rudraswami et al., 2007) and NWA 5697 (L3.10) 5-C10 with  $(4.4\pm1.1)\times10^{-6}$   
719 (Bollard et al., 2019). In addition Semarkona (LL3.00) type I chondrule CH3 containing fine-  
720 grained anorthite show  $(^{26}\text{Al}/^{27}\text{Al})_0$  of  $(7.2\pm2.5)\times10^{-6}$  (Kita et al., 2000, revision by Kita et al.,  
721 2010), which is within the same range observed from other chondrules.

722 The ages determined from the six chondrules from LL chondrites presented here are  
723 indistinguishable ( $1.9\pm0.1$  Ma after CAI formation). In contrast, 8 chondrules in L chondrites show  
724 resolvable ages from 1.8 Ma to 2.2 Ma after CAI formation. The uncertainties in the relative ages  
725 obtained from this study are mostly between 0.04 Ma and 0.10 Ma, which are smaller than those  
726 of previous studies (e.g., Kita et al., 2000; Rudraswami et al., 2007; 2008; Bollard et al., 2019).  
727 The fact that both chondrules analyzed with MCFC and FC-EM methods gave indistinguishable  
728 ages within errors of 0.04-0.07 Ma is a strong evidence that these uncertainties are not  
729 underestimated. Inside this short timescale of 0.4 Ma, there seems to be at least two different  
730 chondrule forming events, with two chondrules from QUE 97008 (c143, c150) at 2.13 and 2.16  
731 Ma and the rest being older. The high MSWD for this degree of freedom (MSWD=1.98, n=14) for  
732 the weighted mean age for all chondrules is also a good indication that there is more than one  
733 population of ages. The hypothesis that the two chondrules belong to the same population than the  
734 rest of chondrules return a welsh t-test p-value that is extremely low (i.e., 0.0002). Similarly, when  
735 taking three different populations, roughly representing the 3 peaks, of  $< 1.95$ ,  $1.95\text{-}2.05$  and  $>$   
736 2.05 Ma, all welsh t-test return p-values well below 0.05. When considered separately, these three  
737 populations give weighted mean age of  $1.86 \pm 0.04$  Ma (2SD, n=9, MSWD=0.77),  $2.02 \pm 0.10$  Ma  
738 (2SD, n=3, MSWD=0.08), and  $2.15 \pm 0.18$  Ma (2SD, n=2, MSWD=0.03), respectively. These  
739 three different populations can be seen very easily on the kernel density function of Fig. 11b.

740 Alternatively, these two youngest chondrules in QUE 97008 (c143, c150) could have been affected  
741 by parent body metamorphism. They both show the relatively lower  $\delta^{26}\text{Mg}^*$  values from data with  
742 highest  $^{27}\text{Al}/^{24}\text{Mg}$  ratios, which could have been caused by loss of excess  $^{26}\text{Mg}$  by diffusion. The  
743 younger chondrules in L seems to correspond to the potential second and third populations at 2.0  
744 Ma and 2.15 Ma described above, which need further targeted studies to confirm because only a  
745 few chondrules were analyzed in each population. Nevertheless, the small number of data points  
746 for each peak is a detriment to any robust statistical analysis that should be completed with more  
747 data.

748 The relationship between type I and II chondrules has been a subject of debate for decades  
749 (Jones, 1990; Villeneuve et al., 2015). Recently, oxidation of type I chondrules has been proposed  
750 as a mechanism for type II chondrule formation (Villeneuve et al., 2015). Such a mechanism would  
751 imply that type II chondrules are younger than type I. Although only four type I chondrules were  
752 measured in this study, this is not what is observed here; type I chondrules show indistinguishable  
753 ages from type II chondrules. In Acfer 094 (ungroup C3.00) and the CO3 chondrite Y-81020, type  
754 II chondrules show systematically  $^{16}\text{O}$ -poor O isotope ratios, compared to type-Is, and frequently  
755 contain  $^{16}\text{O}$ -rich forsteritic relict grains (Kunihiro et al., 2004; 2005; Ushikubo et al., 2012; Tenner  
756 et al., 2013). There are hints of younger Al-Mg ages for type II chondrules than type I chondrules  
757 (Kurahashi et al., 2008), which would at least be consistent with the hypothesis. In contrast, types  
758 I and II plagioclase-bearing chondrules do not show systematic changes in  $\Delta^{17}\text{O}$  with Mg# (Fig.  
759 8b). They were likely formed in the same chondrule forming environments as typical chondrules,  
760 but with different dust-enrichment factors and/or bulk Fe contents that resulted in variable Mg#.  
761 The oxidation of type-I chondrule to form type-II chondrule might also happen in a shorter

762 timescale than the precision of the Al-Mg ages from this study. This preclude any definitive  
763 conclusion on the process of type-II formation using only Al-Mg ages.

764

#### 765 **4.4. Comparison to U-Pb ages**

766

767 Connally et al. (2012) and Bollard et al. (2017) determined Pb-Pb ages of 13 chondrules  
768 from NWA 5697 (L3.10) chondrite, which show ages between 4567.6 Ma to 4563.6 Ma with  
769 uncertainties of 0.3-0.7 Ma. Most chondrules studied by Bollard et al. (2017) contained anorthite,  
770 indicating that they could have been similar to anorthite-bearing chondrules studied here.  
771 Compared to U isotope corrected Pb-Pb ages of CAIs ( $4567.30 \pm 0.13$  Ma), these data indicate that  
772 formation of L chondrite chondrules started contemporaneously to CAI formation and continued  
773 for 4 Ma, in contrast to a narrow range of Al-Mg ages determined in this study. Bollard et al.  
774 (2017) suggested that Pb-Pb ages of chondrules represent the time of last chondrule melting  
775 because they found that U and radiogenic Pb locate in fine-grained mesostasis phases in chondrules  
776 according to SIMS analyses. Therefore, Pb-Pb and Al-Mg systems are supposed to show consistent  
777 ages. Bollard et al. (2019) further obtained SIMS Al-Mg analyses of 7 chondrules in NWA 5697  
778 with known Pb-Pb ages along with bulk Al-Mg measurements using high precision solution ICP-  
779 MS. As mentioned earlier, the initial ( $^{26}\text{Al}/^{27}\text{Al}$ ) ratios determined from isochron regression show  
780 values from  $(4.5 \pm 1.1) \times 10^{-6}$  to  $(8.9 \pm 1.8) \times 10^{-6}$ , which are generally consistent with those obtained  
781 in this work. In resolving the discrepancy of the ranges of chondrule ages between the two  
782 chronometers, Bollard et al. (2019) suggested that  $^{26}\text{Al}$  abundance of chondrule precursors were  
783 heterogeneous that correlate with the absolute ages.

784 Alternatively, the Pb-Pb ages of chondrules would be erroneous by regression of Pb-Pb  
785 isochron using a series of acid leachates from chondrules. Recently, Blichert-Toft et al. (2020)  
786 observed heterogeneous apparent Th/U ratios within and among chondrules in Allende, which  
787 were estimated from the analyses of radiogenic  $^{208}\text{Pb}^*/^{206}\text{Pb}^*$  ratios and might be related to  
788 multiple processes and precursors under variable oxidation state of uranium. They argued that the  
789 linear Pb-Pb isotope regression lines from acid leaching could have been a mixing line rather than  
790 isochron by reflecting multiple processes or precursors. Furthermore, as observed by Bolland et al.  
791 (2017), U and radiogenic Pb locate in mesostasis, because U distribute in chondrule melt rather  
792 than olivine and low-Ca pyroxene phenocrysts. Therefore, radiogenic Pb isotope in chondrules  
793 would not be easily isolated as acid residues, in contrast to coarse grained CAIs and igneous  
794 meteorites that contain Ca-rich pyroxene as a major host of U and radiogenic Pb isotopes. The  
795 Cr<sub>2</sub>O<sub>3</sub> contents of chondrule olivine in NWA 5697 reported by Bolland et al. (2017) vary from  
796 0.1% to 0.5%, which are more variable and systematically lower than those reported from  
797 chondrules in this study (Fig. 4). Such variability in Cr is consistent with higher subtype 3.10 of  
798 NWA 5697 than the chondrites used in this work (3.00-3.05). U-Pb system of fine-grained  
799 mesostasis would be likely disturbed during mild parent body thermal metamorphism, during  
800 which Cr redistribute within olivine. Under such circumstances, Pb-Pb ages of chondrules would  
801 become younger if mesostasis lost radiogenic Pb. Altered mesostasis in chondrules could also gain  
802 radiogenic Pb that had been released from other U-bearing phases and incorporate more  $^{207}\text{Pb}$  due  
803 to shorter half-life of  $^{235}\text{U}$ , which would result in older Pb-Pb ages. In this regard, the Pb-Pb age  
804 of chondrule C3 from NWA 5697 that show highest  $\mu$  value ( $^{238}\text{U}/^{204}\text{Pb}$  ratio) would be more  
805 reliable than those of other chondrules with lower  $\mu$  values. The Pb-Pb age of C3 is  $4566.02 \pm 0.26$   
806 Ma, which is  $2.65 \pm 0.36$  Ma younger than that of D'Orbigny angrite ( $4563.37 \pm 0.25$  Ma; Brennecka

807 et al., 2012). The inferred initial ( $^{26}\text{Al}/^{27}\text{Al}$ ) ratios of NWA 5697 chondrule C3 and D'Orbigny  
808 angrite are  $(8.12 \pm 2.76) \times 10^{-6}$  and  $(5.06 \pm 0.92) \times 10^{-7}$ , respectively, which translate to the time  
809 difference of  $2.82 \pm 0.33$  Ma. It is likely that age mismatch between Pb-Pb and Al-Mg chronometers  
810 in part due to a choice of age anchor between absolute and relative ages.

811

812 **4.5. Timing of UOC chondrule formation**

813

814 The chondrules dated here are all alkali-poor chondrules that are not typical for OC  
815 chondrules, though the  $(^{26}\text{Al}/^{27}\text{Al})_0$  observed from alkali-rich chondrules in the least  
816 metamorphosed chondrites (3.00-3.05) in literature generally show a similar range. Kita et al.  
817 (2000) reported three type II chondrules with glassy mesostasis or Na-rich plagioclase in  
818 Semarkona (LL3.00) and obtained inferred  $(^{26}\text{Al}/^{27}\text{Al})_0$  from  $(4.7 \pm 2.2) \times 10^{-6}$  to  $(9.0 \pm 1.6) \times 10^{-6}$ .  
819 This translate into ages of  $1.79 \pm (^{+0.20/-0.17})$  Ma and  $2.5 \pm (^{+0.6/-0.4})$  Ma after CAIs. Analyses of six  
820 chondrules in LEW 86134 (L3.00) and QUE 97008 (L3.05) by Rudraswani et al. (2007) are at  
821 relatively large uncertainties, though all chondrules show  $(^{26}\text{Al}/^{27}\text{Al})_0$  that are within the range  
822 observed from anorthite-bearing chondrules in this study, except for one chondrule in LEW 86134  
823 with upper limit of  $(^{26}\text{Al}/^{27}\text{Al})_0 < 5.3 \times 10^{-6}$ . Rudraswani et al. (2008) obtained inferred  $(^{26}\text{Al}/^{27}\text{Al})_0$   
824 from  $(1.10 \pm 0.24) \times 10^{-5}$  to  $(5.5 \pm 0.3) \times 10^{-6}$  in the 4 chondrules from Semarkona (LL3.00), all within  
825 the range observed in this study. This translate into ages after CAIs of  $1.59 \pm (^{+0.25/-0.20})$  Ma and  
826  $2.29 \pm 0.06$  Ma. Villeneuve et al. (2009) obtained inferred  $(^{26}\text{Al}/^{27}\text{Al})_0$  from  $(1.62 \pm 0.17) \times 10^{-5}$  to  
827  $(3.0 \pm 1.2) \times 10^{-6}$  from 14 chondrules in Semarkona (LL3.00) with a peak at  $\sim 7 \times 10^{-6}$ , corresponding  
828 to the relative ages from  $1.20 \pm (^{+0.11/-0.10})$  Ma to  $2.90 (^{+0.54/-0.35})$  Ma with a peak at 2.0 Ma after  
829 CAIs. Pape et al. (2019) obtained inferred  $(^{26}\text{Al}/^{27}\text{Al})_0$  from  $(9.5 \pm 2.8) \times 10^{-6}$  to  $(3.1 \pm 1.2) \times 10^{-6}$  from

830 30 UOC (L/LL 3.00-3.15) chondrules (except for one with only upper limit of  $2.6 \times 10^{-6}$  in NWA  
831 8276 Ch2), corresponding to relative ages from  $1.7 \pm 0.3$  Ma to  $2.9^{(+0.5/-0.3)}$  Ma after CAIs. This  
832 dataset shows a peak of  $(^{26}\text{Al}/^{27}\text{Al})_0$  at  $\sim 5.5 \times 10^{-6}$  and  $\sim 7.5 \times 10^{-6}$ , corresponding to ages 2.3 Ma and  
833 2.0 Ma after CAIs. Bollard et al. (2019) analyzed two chondrules with glassy mesostasis in NWA  
834 5697 (L3.10), C1 and C2, show  $(^{26}\text{Al}/^{27}\text{Al})_0$  of  $(8.2 \pm 1.0) \times 10^{-6}$  and  $(8.1 \pm 2.8) \times 10^{-6}$ , respectively,  
835 which exactly match the main peak of the distribution obtained in this study.

836 Villeneuve et al. (2009) and Pape et al. (2019) collected data from typical porphyritic  
837 chondrules with glassy mesostasis in UOCs using high precision MCFC analyses that resulted in  
838 smaller uncertainties for inferred  $(^{26}\text{Al}/^{27}\text{Al})_0$  than those of earlier studies using a single collector  
839 EM (Kita et al., 2000; Rudraswami et al., 2007; 2008). Thus, they are suitable dataset to compared  
840 Al-Mg ages between Na-depleted anorthite-bearing chondrules in this study and normal Na-rich  
841 chondrules in UOCs. Their results indicated a peak at 2.0 Ma, which is generally consistent with  
842 our results, though they show a broader age distribution that include many chondrules with ages  
843 2.3 Ma or younger. In total 44 chondrules in L/LL 3.00-3.05 UOCs studied by Villeneuve et al.  
844 (2009) and Pape et al. (2019), 8 chondrules show inferred  $(^{26}\text{Al}/^{27}\text{Al})_0$  that are outside of observed  
845 range of this study beyond analytical uncertainties; 2 chondrule are higher and 6 are lower  
846 including one that only show the upper limit. The discrepancy of age distribution between  
847 anorthite-bearing chondrules and normal chondrules in UOCs would be related to different  
848 formation environments and timing between two suites of chondrules that show distinct chemical  
849 natures. Here we focused on alkali-poor chondrules which are unusual in UOCs, while Villeneuve  
850 et al. (2009) and Pape et al. (2019) analyzed a much wider range of chondrule types and mesostasis  
851 compositions. Alkali-poor chondrule might have formed at a different time in the solar nebula and  
852 during a much more restricted timescale.

853                   Alternatively, large spot analyses employed by Villeneuve et al. (2009) and Pape et al.  
854 (2019) could have been affected by parent body metamorphism and/or alterations. Even in  
855 Semarkona (3.00), aqueous alteration at low temperatures resulted in minor occurrence of clay  
856 minerals in chondrule mesostasis (Grossman et al., 2000; Lewis et al., 2019). SIMS analyses that  
857 overlap multiple phases may result in disturbed Al-Mg isochron by including such altered grain  
858 boundaries where radiogenic  $^{26}\text{Mg}$  could have been lost. The isochron regressions of some  
859 chondrules determined by Villeneuve et al. (2009) and Pape et al. (2019) show a significantly large  
860 scatter with high MSWD values of 4-5, which were never observed in this study ( $\leq 2$ ). Recently,  
861 the potential bias of data from regressions with high MSWD has been highlighted for initial  
862  $^{10}\text{Be}/^{9}\text{Be}$  ratios (Dunham et al., 2020). A similar, high precision SIMS analyses by targeting clean  
863 Na-rich plagioclase in more typical Na-rich chondrules form UOCs is required to further clarify  
864 the entire Al-Mg age distribution of UOCs with the new capabilities offered from the new RF ion  
865 source.

866                   Alexander et al. (2008) and Alexander and Ebel (2012) argued that ordinary chondrite  
867 chondrules formed in extremely dense environments, which could have had sufficient self-gravity  
868 to collapse spontaneously (Alexander et al., 2008), so that UOC chondrules from a single group  
869 should show a very narrow formation period, likely  $< 0.1$  Ma. By taking only the oldest population  
870 of chondrules ( $1.86 \pm 0.04$  Ma), our data may support their hypothesis. However, taking all data  
871 in Fig. 11, we do find resolvable ages among chondrules that range from 1.8 Ma to 2.2 Ma.  
872 Including other literature data from normal chondrules in UOCs (e.g., Villeneuve et al., 2009; Pape  
873 et al., 2019), the total range of chondrule ages are even larger. It is possible that anorthite-bearing  
874 chondrules formed earlier in a dust-rich environment, but not as dense as indicated by Alexander  
875 et al. (2008). As discussed earlier, the Al-Mg ages of Na-rich porphyritic chondrules (Villeneuve

876 et al., 2009; Pape et al., 2019) may not be significantly different from those of the anorthite-bearing  
877 chondrules in this study. Therefore, Na-rich chondrule formation under extreme dust-enrichment  
878 might have postdated the formation of the majority of anorthite bearing chondrules at  $1.9 \pm 0.1$   
879 Ma, formed during the first event, and might have been concurrent with the formation of the  
880 younger anorthite-bearing chondrules at 2.0 Ma to 2.15 Ma. It is interesting to note that youngest  
881 ages reported in this study are similar to the age estimated for parent body accretion in several  
882 studies (Sugiura and Fujiya, 2014; Blackburn et al., 2017), in which abundance of  $^{26}\text{Al}$  at the time  
883 of accretion is one of the important parameters to determine thermal evolution of the asteroidal  
884 bodies. Blackburn et al. (2017) estimated the accretion time of H and L chondrites to be from 2.05  
885 Ma to 2.25 Ma after CAIs. UOC chondrule ages that are significantly younger than 2.3 Ma after  
886 CAIs may not be consistent with the timing of parent body formation expected from thermal  
887 model. Future study may focus on determination of youngest chondrules in UOC and careful  
888 evaluation of the extents of parent body metamorphism on the Al-Mg system.

889

## 890 5. CONCLUSION

891

892 In this study we determined the  $(^{27}\text{Al}/^{26}\text{Al})_0$  of 14 anorthite bearing chondrules from 5  
893 different unequilibrated ordinary chondrites (UOCs), with a wide range of chondrule types and  
894 compositions. New analytical development using a multi-collection FC-EM detector configuration  
895 allows for the precise measurements of excess  $^{26}\text{Mg}$  in plagioclase at the level of  $\pm 0.5\text{--}0.7\text{\%}$  from  
896 a single 6  $\mu\text{m}$  SIMS spot analyses. Multi-collection FC (MCFC) analyses with a spot size of  $\sim 15$   
897  $\mu\text{m}$  allow for 0.3-0.4% uncertainty. These improved analytical precisions allow us to determine  
898 Al-Mg ages of chondrules with precisions better than 0.1 Ma. We conclude the following:

899 1) Anorthite bearing chondrules show a wide range of Mg# and textural relationships between  
900 olivine/pyroxene and anorthites. Some show mineral and compositional zoning indicative  
901 of crystallization from the rim inwards, suggesting that they are not fragments of former  
902 differentiated objects, but instead a minor group of chondrules uniquely found in L and LL  
903 chondrites. Anorthite in these chondrules show silica excess and relatively high MgO  
904 contents, indicating that they preserved their primary high temperature characteristics.

905 2) All chondrules show resolvable  $\delta^{26}\text{Mg}^*$  and yield Al-Mg isochrons with acceptable  
906 MSWD. Their  $(^{27}\text{Al}/^{26}\text{Al})_0$  range from  $(6.3 \pm 0.4) \times 10^{-6}$  to  $(8.9 \pm 0.2) \times 10^{-6}$ . Assuming a  
907 homogeneous distribution of  $^{26}\text{Al}$  in the Solar System with a canonical  $(^{27}\text{Al}/^{26}\text{Al})_0$  value  
908 of  $5.25 \times 10^{-5}$  at the time of CAI formation, these chondrule formed from  $1.80 \pm 0.04$  to  
909  $2.16 \pm 0.11$  Ma after CAIs.

910 3) The formation ages of anorthite-bearing chondrules are at the peak of those of normal Na-  
911 rich chondrules, though the timescale for chondrule formation reported in this study of  $<$   
912  $0.4$  Ma is much shorter than those estimated by Villeneuve et al. (2009) and Pape et al.  
913 (2019). The youngest age observed from this study is consistent with the estimated time of  
914 accretion of ordinary chondrite parent bodies (e.g., Blackburn et al., 2017).

915 4) Resolvable ages among chondrules in this study indicate that chondrules did not form  
916 during a single event, but potentially 2 or 3 discrete chondrule forming events. These  
917 different events might not have been coeval for L and LL chondrites since all younger ages  
918 are found for chondrules in L chondrites. This is not consistent with the very short duration  
919 ( $<0.1$  Ma) expected from extremely dense chondrule forming environments, which might  
920 not be applied to Na-depleted anorthite bearing chondrules in this study.

921  
922

923

## ACKNOWLEDGMENTS

924

925        We thank Steve Simon, Timothy McCoy, and ANSMET program for allocation of  
926        meteorite samples. We acknowledge extensive supports from John Fournelle for EPMA, and Bill  
927        Schneider for SEM, and Michael Spicuzza for SIMS. Michael Spicuzza reviewed an earlier version  
928        of this manuscript. Constructive reviews were provided by Conel Alexander, anonymous  
929        reviewers, and associate editor Anders Meibom, which improved the quality of the manuscript.  
930        This work is supported by NASA Emerging World Program (NNX17AE29G, N. K.). The upgrade  
931        of the RF plasma ion source is supported by the NASA Laboratory Analysis of Returned Samples  
932        and Planetary Major Equipment Programs (NNX16AG80G) and the NSF Instrumentation and  
933        Facility Program (EAR-1355590). WiscSIMS is partly supported by NSF (EAR-1658823). FIB  
934        instrumentation was supported by NSF through the University of Wisconsin Materials Research  
935        Science and Engineering Center (DMR-17204015).

936

937

## RESEARCH DATA

938

939        Research data is stored as Mendeley dataset and can be found using the following link:

940        <http://dx.doi.org/10.17632/f3s69sjg6k.4>

941

942

943

## REFERENCES

944

945 Alexander C. M. O. (2005) From Supernovae to Planets: The View from Meteorites and  
946 Interplanetary Dust Particles. In (eds. A. N. Krot and E. R. D. Scott). ASP Conference  
947 Series. pp. 972–1002.

948 Alexander C. M. O. and Ebel D. S. (2012) Questions, questions: Can the contradictions between  
949 the petrologic, isotopic, thermodynamic, and astrophysical constraints on chondrule  
950 formation be resolved? *Meteoritics & Planetary Science* **47**, 1157–1175.

951 Alexander C. M. O., Barber D. J. and Hutchison R. (1989) The microstructure of Semarkona and  
952 Bishunpur. *Geochimica et Cosmochimica Acta* **53**, 3045–3057.

953 Alexander C. M. O., Grossman J. N., Ebel D. S. and Ciesla F. J. (2008) The Formation  
954 Conditions of Chondrules and Chondrites. *Science* **320**, 1617–1619.

955 Anon (2014) Comment on Bybee et al. (2014): Pyroxene megacrysts in Proterozoic anorthosites:  
956 Implications for tectonic setting, magma source and magmatic processes at the Moho. *Earth  
957 and Planetary Science Letters* **401**, 378–380.

958 Beatty D. W. and Albee A. L. (1980) Silica solid solution and zoning in natural plagioclase.  
959 *American Mineralogist* **65**, 63–74.

960 Berlin J., Jones R. H. and Brearley A. J. (2011) Fe-Mn systematics of type IIA chondrules in  
961 unequilibrated CO, CR, and ordinary chondrites. *Meteoritics & Planetary Science* **46**, 513–  
962 533.

963 Blackburn T., Alexander C. M. O., Carlson R. and Elkins-Tanton L. T. (2017) The accretion and  
964 impact history of the ordinary chondrite parent bodies. *Geochimica et Cosmochimica Acta*  
965 **200**, 201–217.

966 Blichert-Toft J., Göpel C., Chaussidon M., Albarède F. (2020) Th/U variability in Allende  
967 chondrules. *Geochimica et Cosmochimica Acta* **280**, 378–394.

968 Bollard J., Connelly J. N., Whitehouse M. J., Pringle E. A., Bonal L., Jørgensen J. K., Nordlund  
969 Å., Moynier F. and Bizzarro M. (2017) Early formation of planetary building blocks inferred  
970 from Pb isotopic ages of chondrules. *Sci. Adv.* **3**, 1–10.

971 Bollard J., Kawasaki N., Sakamoto N., Olsen M., Itoh S., Larsen K., Wielandt D., Schiller M.,  
972 Connelly J. N., Yurimoto H. and Bizzarro M. (2019) Combined U-corrected Pb-Pb dating  
973 and 26Al-26Mg systematics of individual chondrules – Evidence for a reduced initial  
974 abundance of 26Al amongst inner Solar System chondrules. *Geochimica et Cosmochimica  
975 Acta* **260**, 62–83.

976 Bruno E. and Facchinelli A. (1975) Crystal-chemical interpretation of crystallographic anomalies  
977 in lunar plagioclases. *bulmi* **98**, 113–117.

978 Brenneka G. A. and Wadhwa M. (2012) Uranium isotope compositions of the basaltic angrite  
979 meteorites and the chronological implications for the early Solar System. *PNAS* **109**, 9299–  
980 9303.

981 Budde G., Kruijer T. S. and Kleine T. (2018) Hf-W chronology of CR chondrites: Implications  
982 for the timescales of chondrule formation and the distribution of 26Al in the solar nebula.  
983 *Geochimica et Cosmochimica Acta* **222**, 284–304.

984 Catanzaro E. J., Murphy T. J., Garner E. L. and Shields W. R. (1966) Absolute isotopic  
985 abundance ratios and atomic weight of magnesium. *Journal of Research of the National  
986 Bureau of Standards* **70A**, 453–458.

987 Clayton R. N., Mayeda T. K., Goswami J. N. and Olsen E. J. (1991) Oxygen isotope studies of  
988 ordinary chondrites. *Geochimica et Cosmochimica Acta* **55**, 2317–2337.

989 Connelly J. N., Bizzarro M., Krot A. N., Nordlund A., Wielandt D. and Ivanova M. A. (2012)  
990 The Absolute Chronology and Thermal Processing of Solids in the Solar Protoplanetary  
991 Disk. *Science* **338**, 651–655.

992 Cuzzi J. N., Hogan R. C. and Bottke W. F. (2010) Towards initial mass functions for asteroids  
993 and Kuiper Belt Objects. *Icarus* **208**, 518–538.

994 Davis A. M., Richter F. M., Mendybaev R. A., Janney P. E., Wadhwa M. and McKeegan K. D.  
995 (2015) Isotopic mass fractionation laws for magnesium and their effects on 26Al–26Mg  
996 systematics in solar system materials. *Geochimica et Cosmochimica Acta* **158**, 245–261.

997 Desch S. J., Morris M. A., Connolly H. C. Jr and Boss A. P. (2012) The importance of  
998 experiments: Constraints on chondrule formation models. *Meteoritics & Planetary Science*  
999 **47**, 1139–1156.

1000 Donovan J. J., Singer J. W. and Armstrong J. T. (2016) A new EPMA method for fast trace  
1001 element analysis in simple matrices. *American Mineralogist* **101**, 1839–1853.

1002 Dunham E. T., Wadhwa M., Desch S. J. and Hervig R. L. (2020) Best Practices for  
1003 Determination of Initial  $^{10}\text{Be}$ /  $^{9}\text{Be}$  in Early Solar System Materials by Secondary Ion Mass  
1004 Spectrometry. *Geostand Geoanal Res* **52**, 1–16.

1005 Fukuda K., Brownlee D. E., Joswiak D. J., Tenner T. J., Kimura M. and Kita N. T. (2020)  
1006 Correlated isotopic and chemical evidence for condensation origins of olivine in comet  
1007 81P/Wild 2 and in AOAs from CV and CO chondrites. *Geochimica et Cosmochimica Acta*,  
1008 1–65.

1009 Fukuda K., Beard B. L., Dunlap D. R., Spicuzza M. J., Fournelle J. H., Wadhwa M. and Kita N.  
1010 T. (2020) Magnesium isotope analysis of olivine and pyroxene by SIMS: Evaluation of  
1011 matrix effects. *Chemical Geology* **540**, 119482.

1012 Grossman J. N. (1988) Chondrites and the solar nebula. *Nature* **334**, 14–15.

1013 Grossman J. N. and Brearley A. J. (2005) The onset of metamorphism in ordinary and  
1014 carbonaceous chondrites. *Meteoritics & Planetary Science* **40**, 87–122.

1015 Hertwig A. T., Kimura M., Ushikubo T., Defouilloy C. and Kita N. T. (2019) The  $^{26}\text{Al}$ - $^{26}\text{Mg}$   
1016 systematics of FeO-rich chondrules from Acfer 094: Two chondrule generations distinct in  
1017 age and oxygen isotope ratios. *Geochimica et Cosmochimica Acta* **253**, 111–126.

1018 Hutcheon I. D. and Hutchison R. (1989) Evidence from the Semarkona ordinary chondrite for  
1019  $^{26}\text{Al}$  heating of small planets. *Letters to Nature* **337**, 238–241.

1020 Hutcheon I. D. and Jones R. H. (1995) The  $^{26}\text{Al}$ - $^{26}\text{Mg}$  record of chondrules: clues to nebular  
1021 chronology. *Lunar and Planetary Sciences* **25**, 587–588.

1022 Isa J., Kohl I. E., Liu M. C., Wasson J. T., Young E. D. and McKeegan K. D. (2017)

1023 Quantification of oxygen isotope SIMS matrix effects in olivine samples: Correlation with

1024 sputter rate. *Chemical Geology* **458**, 14–21.

1025 Jacobsen B., Yin Q.-Z., Moynier F., Amelin Y., Krot A. N., Nagashima K., Hutcheon I. D. and

1026 Palme H. (2008) 26Al–26Mg and 207Pb–206Pb systematics of Allende CAIs: Canonical

1027 solar initial 26Al/27Al ratio reinstated. *Earth and Planetary Science Letters* **272**, 353–364.

1028 Jones R. H. (2012) Petrographic constraints on the diversity of chondrule reservoirs in the

1029 protoplanetary disk. *Meteoritics & Planetary Science* **47**, 1176–1190.

1030 Jones R. H. (1990) Petrology and mineralogy of Type II, FeO-rich chondrules in Semarkona

1031 (LL3.0): Origin by closed-system fractional crystallization, with evidence for supercooling.

1032 *Geochimica et Cosmochimica Acta* **54**, 1785–1802.

1033 Jones R. H. (1994) Petrology of FeO-poor, porphyritic pyroxene chondrules in the Semarkona

1034 chondrite. *Geochimica et Cosmochimica Acta* **58**, 5325–5340.

1035 Kimura M., Grossman J. N. and Weisberg M. K. (2008) Fe-Ni metal in primitive chondrites:

1036 Indicators of classification and metamorphic conditions for ordinary and CO chondrites.

1037 *Meteoritics & Planetary Science* **43**, 1161–1177.

1038 Kita N. T. and Ushikubo T. (2012) Evolution of protoplanetary disk inferred from 26Al

1039 chronology of individual chondrules. *Meteoritics & Planetary Science* **47**, 1108–1119.

1040 Kita N. T., Hertwig A. T., Defouilloy C., Kitajima K. and Spicuzza M. J. (2018) Improvements  
1041 of SIMS Mg isotope analyses for meteoritic and cometary samples using RF plasma ion  
1042 source. In *50th Lunar and Planetary Science Conference*. #2441.

1043 Kita N. T., Nagahara H., Tachibana S., Tomomura S., Spicuzza M. J., Fournelle J. H. and Valley  
1044 J. W. (2010) High precision SIMS oxygen three isotope study of chondrules in LL3  
1045 chondrites: Role of ambient gas during chondrule formation. *Geochimica et Cosmochimica  
1046 Acta* **74**, 6610–6635.

1047 Kita N. T., Nagahara H., Togashi S. and Morishita Y. (2000) A short duration of chondrule  
1048 formation in the solar nebula: Evidence from  $^{26}\text{Al}$  in Semarkona ferromagnesian chondrules.  
1049 *Geochimica et Cosmochimica Acta* **64**, 3913–3922.

1050 Kita N. T., Ushikubo T., Fu B. and Valley J. W. (2009) High precision SIMS oxygen isotope  
1051 analysis and the effect of sample topography. *Chemical Geology* **264**, 43–57.

1052 Kita N. T., Ushikubo T., Knight K. B., Mendybaev R. A., Davis A. M., Richter F. M. and  
1053 Fournelle J. H. (2012) Internal  $^{26}\text{Al}$ - $^{26}\text{Mg}$  isotope systematics of a Type B CAI: Remelting of  
1054 refractory precursor solids. *Geochimica et Cosmochimica Acta* **86**, 37–51.

1055 Kita N. T., Yin Q.-Z., MacPherson G. J., Ushikubo T., Jacobsen B., Nagashima K., Kurahashi  
1056 E., Krot A. N. and Jacobsen S. B. (2013)  $^{26}\text{Al}$ - $^{26}\text{Mg}$  isotope systematics of the first solids  
1057 in the early solar system. *Meteoritics & Planetary Science* **48**, 1383–1400.

1058 Kita N. T., Siron G. and Kimura M. (2019) Petrographic examination of unequilibrated ordinary  
1059 chondrites with low petrologic subtypes. *metsoc.* #6237.

1060 Kunihiro Tak, Rubin A. E. and Wasson J. T. (2005) Oxygen-isotopic compositions of low-FeO  
1061 relicts in high-FeO host chondrules in Acfer 094, a type 3.0 carbonaceous chondrite closely  
1062 related to CM. *Geochimica et Cosmochimica Acta* **69**, 3831–3840.

1063 Kunihiro Takuya, Rubin A. E., McKeegan K. D. and Wasson J. T. (2004) Oxygen-isotopic  
1064 compositions of relict and host grains in chondrules in the Yamato 81020 CO3.0.  
1065 *Geochimica et Cosmochimica Acta* **68**, 3599–3606.

1066 Kurahashi E., Kita N. T., Nagahara H. and Morishita Y. (2008)  $^{26}\text{Al}$ – $^{26}\text{Mg}$  systematics of  
1067 chondrules in a primitive CO chondrite. *Geochimica et Cosmochimica Acta* **72**, 3865–3882.

1068 Larsen K. K., Schiller M. and Bizzarro M. (2016) Accretion timescales and style of asteroidal  
1069 differentiation in an 26Al-poor protoplanetary disk. *Geochimica et Cosmochimica Acta* **176**,  
1070 295–315.

1071 Larsen K. K., Trinquier A., Paton C., Schiller M., Wielandt D., Ivanova M. A., Connelly J. N.,  
1072 Nordlund Å., Krot A. N. and Bizzarro M. (2011) Evidence for magnesium isotope  
1073 heterogeneity in the solar protoplanetary disk. *ApJ* **735**, L37–7.

1074 Longhi J. and Hays J. F. (1979) Phase equilibria and solid solution along the join  $\text{CaAl}_2\text{Si}_2\text{O}_8$ –  
1075  $\text{SiO}_2$ . *American Journal of Science* **279**, 876–890.

1076 Longhi J., Walker D. and Hays J. F. (1976) Fe and Mg plagioclase. *Proc. Lunar Sci. Conf. 7th*,  
1077 1281–1300.

1078 MacPherson G. J. and Huss G. R. (2005) Petrogenesis of Al-rich chondrules: Evidence from bulk  
1079 compositions and phase equilibria. *Geochimica et Cosmochimica Acta* **69**, 3099–3127.

1080 Mittlefehldt D. W. and Berger E. L. (2017) Excess silica substitution in plagioclase grains in the  
1081 Pasamonte eucrite. *Meteorit. Planet. Sci.*, 1–1.

1082 Mostefaoui S., Kita N. T., Togashi S., Tachibana S., Nagahara H. and Morishita Y. (2002) The  
1083 relative formation ages of ferromagnesian chondrules inferred from their initial aluminum-  
1084 26/aluminum-27 ratios. *Meteoritics & Planetary Science* **37**, 421–438.

1085 Nishiizumi K. (2004) Preparation of 26Al AMS standards. *Nuclear Instruments and Methods in  
1086 Physics Research Section B: Beam Interactions with Materials and Atoms* **223-224**, 388–  
1087 392.

1088 Pape J., Mezger K., Bouvier A. S. and Baumgartner L. P. (2019) Time and Duration of  
1089 Chondrule Formation: Constraints from 26Al-26Mg Ages of Individual Chondrules.  
1090 *Geochimica et Cosmochimica Acta* **244**, 416–436.

1091 Rudraswami N. G. and Goswami J. N. (2007) 26Al in chondrules from unequilibrated L  
1092 chondrites: Onset and duration of chondrule formation in the early solar system. *Earth and  
1093 Planetary Science Letters* **257**, 231–244.

1094 Rudraswami N. G., Goswami J. N., Chattopadhyay B., Sengupta S. K. and Thapliyal A. P.  
1095 (2008) 26Al records in chondrules from unequilibrated ordinary chondrites: II. Duration of  
1096 chondrule formation and parent body thermal metamorphism. *Earth and Planetary Science  
1097 Letters* **274**, 93–102.

1098 Russell S. S., Huss G. R., MacPherson G. J. and Wasserburg G. J. (1997) Early and late  
1099 chondrule formation: new constraints for solar nebula chronology from 26Al/27Al in  
1100 unequilibrated ordinary chondrites. In *28th Lunar and Planetary Science Conference*. #1468.

1101 Russell S. S., Srinivasan G., Huss G. R., Wasserburg G. J. and MacPherson G. J. (1996)

1102 Evidence for Widespread 26Al in the Solar Nebula and Constraints for Nebula Time Scales.

1103 *Science* **273**, 757–762.

1104 Spear F. S., Rumble D. III and Ferry J. M. (1982) Linear algebraic manipulation of n-

1105 dimensional composition space. *Reviews in Mineralogy and Geochemistry* **10**, 53–104.

1106 Sugiura N. and Fujiya W. (2014) Correlated accretion ages and  $\epsilon$  54Cr of meteorite parent bodies

1107 and the evolution of the solar nebula. *Meteoritics & Planetary Science* **49**, 772–787.

1108 Tachibana S., Nagahara H., Mostefaoui S. and Kita N. T. (2003) Correlation between relative

1109 ages inferred from 26Al and bulk compositions of ferromagnesian chondrules in least

1110 equilibrated ordinary chondrites. *Meteoritics & Planetary Science* **38**, 939–962.

1111 Tenner T. J., Nakashima D., Ushikubo T., Tomioka N., Kimura M., Weisberg M. K. and Kita N.

1112 T. (2019) Extended chondrule formation intervals in distinct physicochemical environments:

1113 Evidence from Al-Mg isotope systematics of CR chondrite chondrules with unaltered

1114 plagioclase. *Geochimica et Cosmochimica Acta* **260**, 133–160.

1115 Tenner T. J., Ushikubo T., Kurahashi E., Kita N. T. and Nagahara H. (2013) Oxygen isotope

1116 systematics of chondrule phenocrysts from the CO3.0 chondrite Yamato 81020: Evidence

1117 for two distinct oxygen isotope reservoirs. *Geochimica et Cosmochimica Acta* **102**, 226–245.

1118 Thompson J. B. (1982) Compositional space: An algebraic and geometric approach. *Reviews in*

1119 *Mineralogy and Geochemistry* **10**, 1–32.

1120 Ushikubo T., Kimura M., Kita N. T. and Valley J. W. (2012) Primordial oxygen isotope  
1121 reservoirs of the solar nebula recorded in chondrules in Acfer 094 carbonaceous chondrite.  
1122 *Geochimica et Cosmochimica Acta* **90**, 242–264.

1123 Ushikubo T., Tenner T. J., Hiyagon H. and Kita N. T. (2017) A long duration of the  $^{16}\text{O}$ -rich  
1124 reservoir in the solar nebula, as recorded in fine-grained refractory inclusions from the least  
1125 metamorphosed carbonaceous chondrites. *Geochimica et Cosmochimica Acta* **201**, 103–122.

1126 Valley J. W. and Kita N. T. (2009) In situ oxygen isotope geochemistry by ion microprobe.  
1127 *Mineralogical Association of Canada Short Course* **41**, 19–63.

1128 Van Orman J. A., Cherniak D. J. and Kita N. T. (2014) Magnesium diffusion in plagioclase:  
1129 Dependence on composition, and implications for thermal resetting of the  $^{26}\text{Al}$ – $^{26}\text{Mg}$  early  
1130 solar system chronometer. *Earth and Planetary Science Letters* **385**, 79–88.

1131 Vermeesch P. (2018) IsoplotR: A free and open toolbox for geochronology. *Geoscience  
1132 Frontiers* **9**, 1479–1493.

1133 Villeneuve J., Chaussidon M. and Libourel G. (2009) Homogeneous Distribution of  $^{26}\text{Al}$  in the  
1134 Solar System from the Mg Isotopic Composition of Chondrules. *Science* **325**, 985–988.

1135 Villeneuve J., Libourel G. and Soulié C. (2015) Relationships between type I and type II  
1136 chondrules: Implications on chondrule formation processes. *Geochimica et Cosmochimica  
1137 Acta* **160**, 277–305.

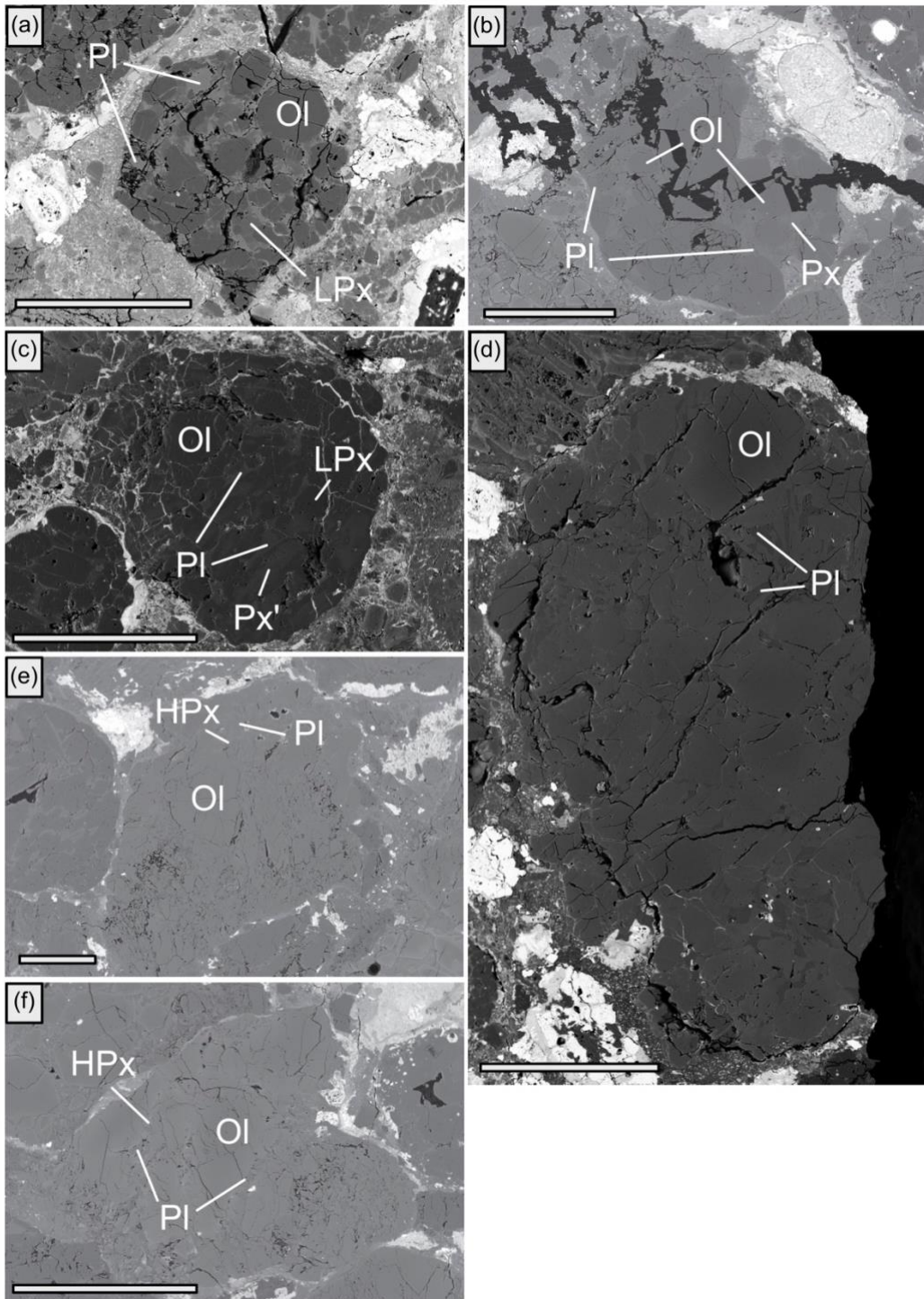
1138 Weil D. F., McCallum I. S., Bottinga Y., Drake M. J. and McKay G. A. (1970) Mineralogy and  
1139 petrology of some Apollo 11 igneous rocks. *Proceedings of the Apollo Lunar Science*  
1140 *Conference* **1**, 937–955.

1141 Wenk H.-R. and Wilde W. R. (1973) Chemical Anomalies of Lunar Plagioclase, Described by  
1142 Substitution Vectors and Their Relation to Optical and Structural Properties. *Contrib*  
1143 *Mineral Petrol* **41**, 89–104.

1144 York D., Evensen N. M., Martínez M. L. and De Basabe Delgado J. (2004) Unified equations for  
1145 the slope, intercept, and standard errors of the best straight line. *American Journal of Physics*  
1146 **72**, 367–375.

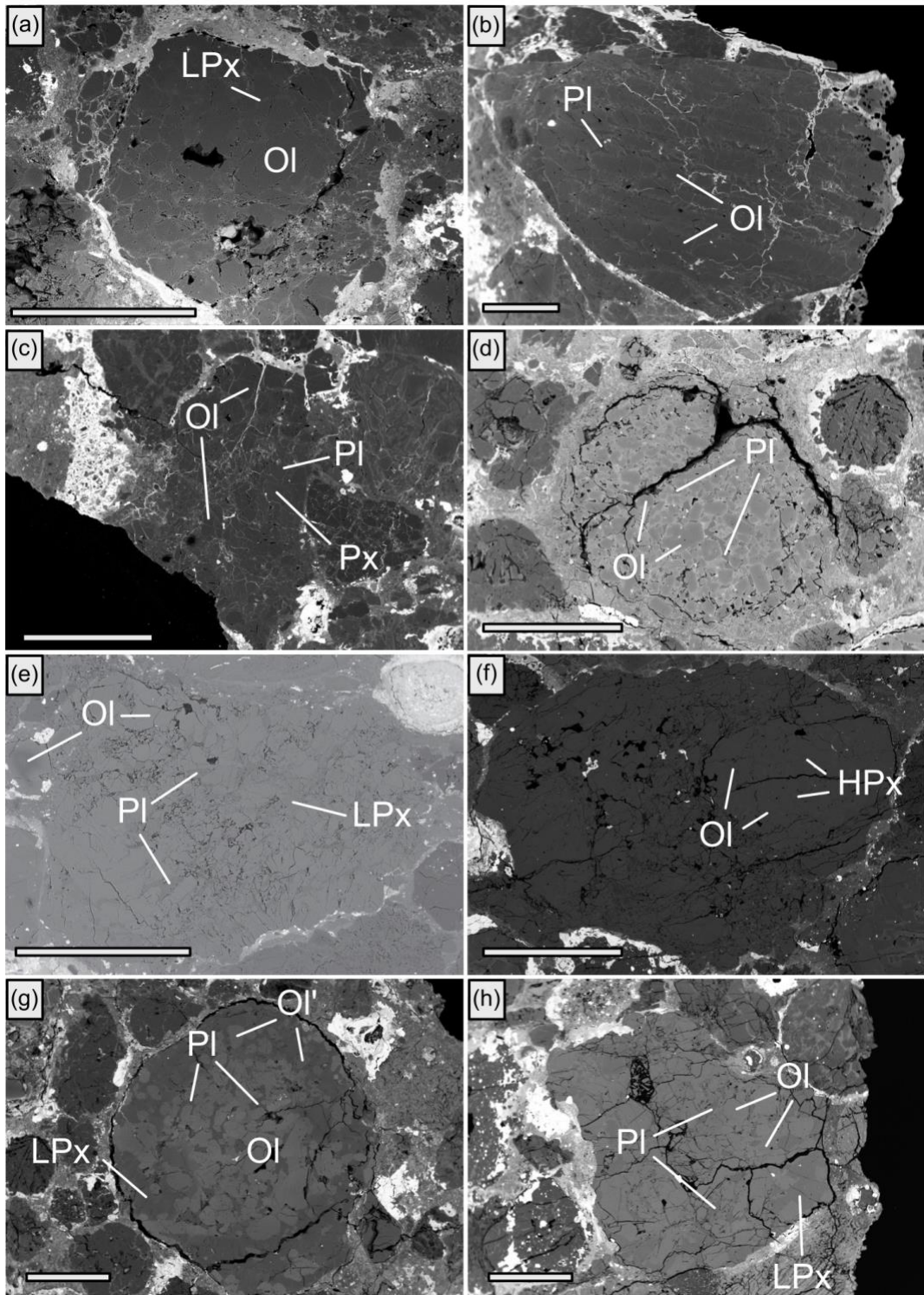
1147  
1148  
1149

### **Figure captions**



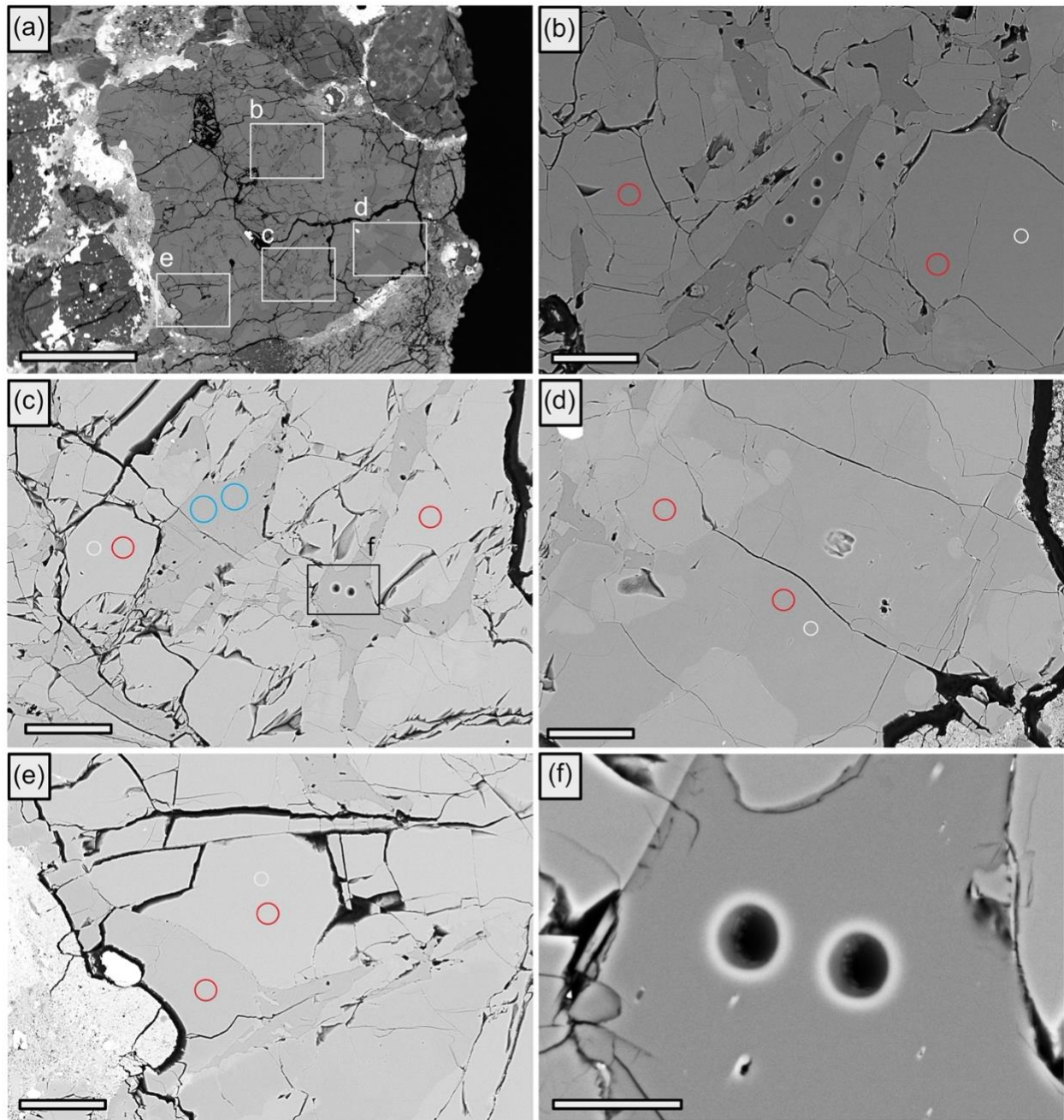
1150

1151 Fig. 1: BSE images of 6 different chondrules. a) NWA8276 c69 (type I-POP), b) QUE97008 c61 (type I-  
 1152 POP), c) NWA8649 c17 (Type I-PP), d) NWA8276 c7 (type II-PO), e) QUE97008 c51 (type II-PO), f)  
 1153 QUE97008 c143 (type II-PO). Mineral abbreviations are as follows: olivine (OI), low-Ca pyroxenes (LPx),  
 1154 high-Ca pyroxenes (HPx), pyroxenes with various amount of Ca (Px), plagioclase (PI); Px' for NWA 8649  
 1155 c17 denotes pyroxene cores that are slightly enriched in Ca compare to low-Ca rims. Scale bar is 500  $\mu$ m.  
 1156 See text for a more detailed description of the different phases and compositions.



1157  
1158  
1159  
1160  
1161  
1162

Fig. 2: BSE images of 8 different chondrules. a) NWA8649 c87 (type II-PO), b) MET00452 c19 (type II-PO), c) MET00452 c111 (type II-POP), d) NWA8276 c87 (type II-PO), e) QUE97008 c150 (type II-PO), f) Semarkona c47 (type II-PO), g) NWA8276 c88 (type II-POP), h) Semarkona c34 (type II-POP). Mineral abbreviations are the same as those in Fig. 1. Olivine inclusions in NWA8276 c88 is shown as (OI'). Scale bar is 500  $\mu$ m. See text for a more detailed description of the different phases and compositions.



1163  
1164  
1165  
1166  
1167  
1168

Fig. 3: Example of chondrule petrography (Semarkona c34), with locations of the different type of analyses made. Red spots refer to the locations of oxygen isotope analyses, white spots are for olivine-pyroxene Al-Mg isotope analyses, blue spots correspond to locations of anorthite MCFC analyses and visible spots are actual spots of FC-EM analyses of anorthite grains.

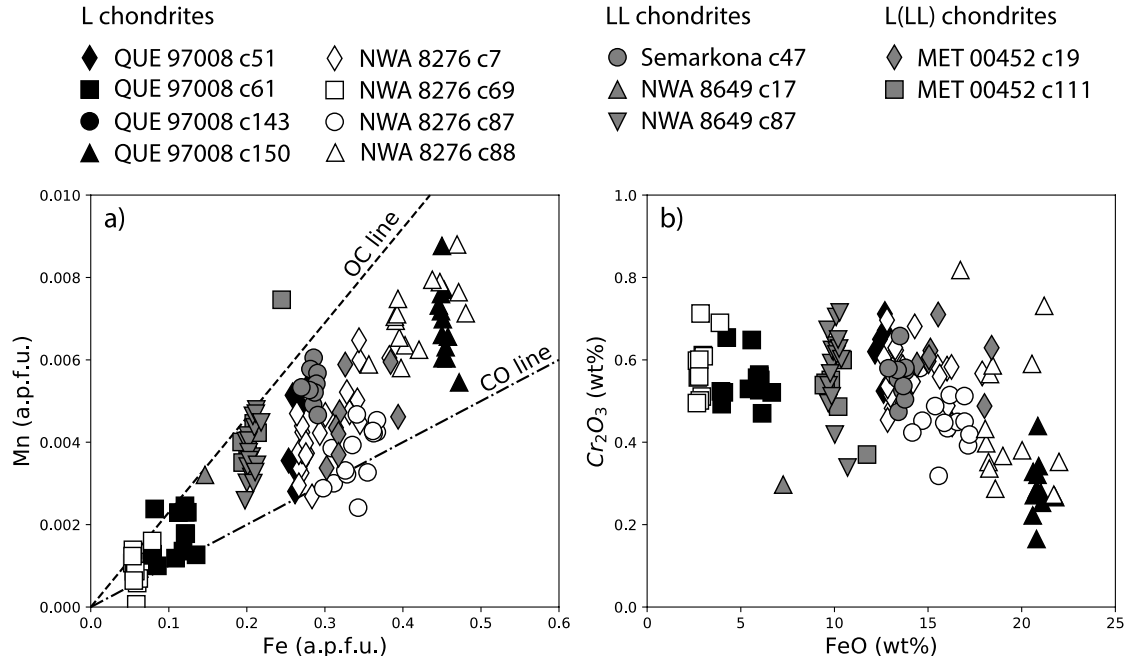


Fig. 4: Composition of olivine analyses from the studied chondrules. a) Fe (a.p.f.u.) vs Mn (a.p.f.u.) diagram with OC (chondrule olivines from ordinary chondrites) and CO (chondrule olivines from CO chondrites) lines from Berlin et al. (2011). b) FeO (wt%) vs Cr<sub>2</sub>O<sub>3</sub> (wt%) diagram. a.p.f.u = atoms per formula unit.

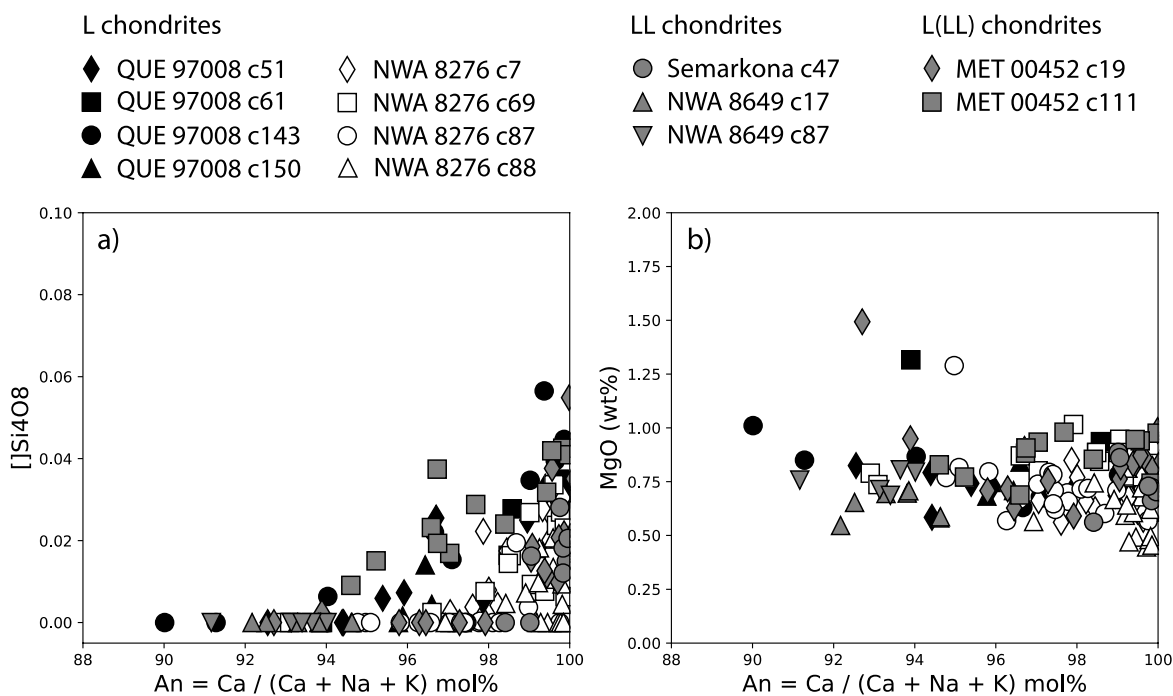
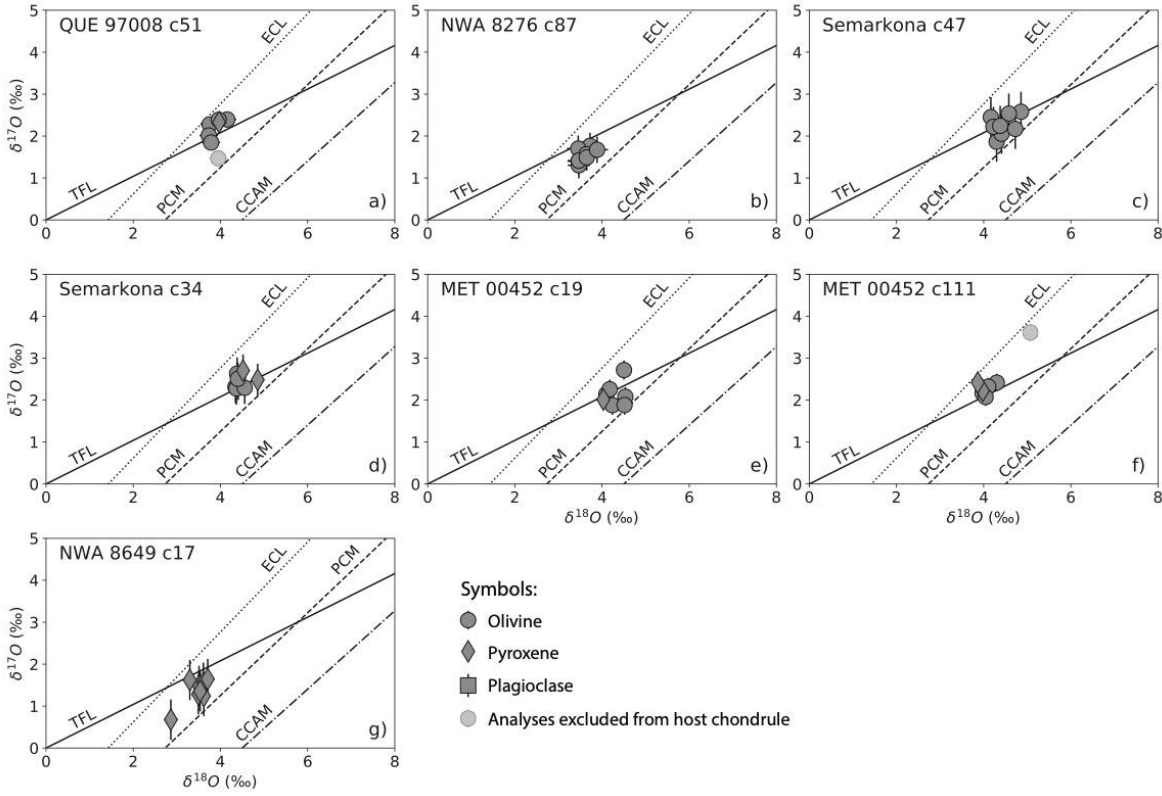
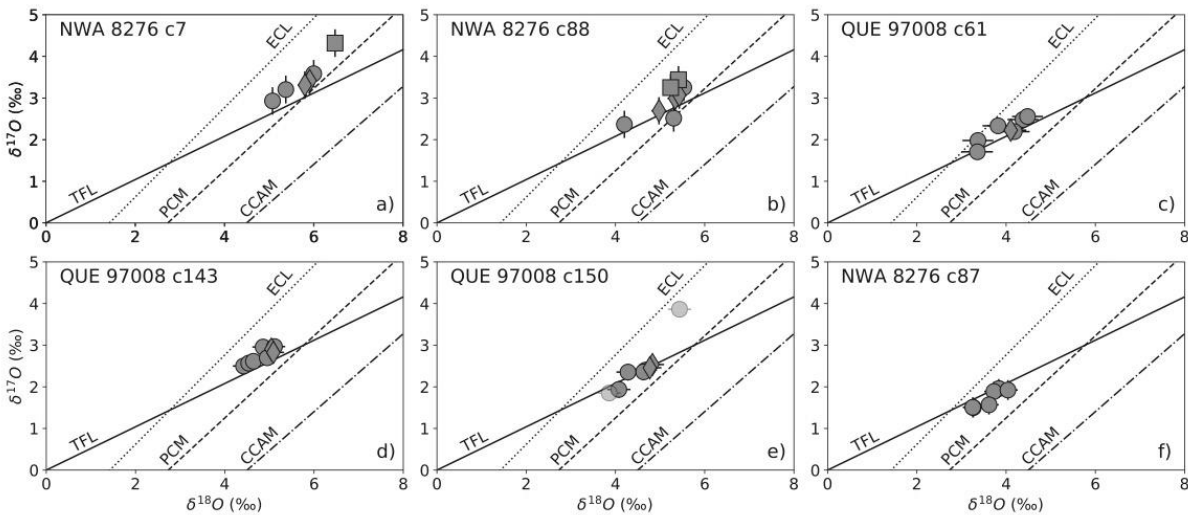


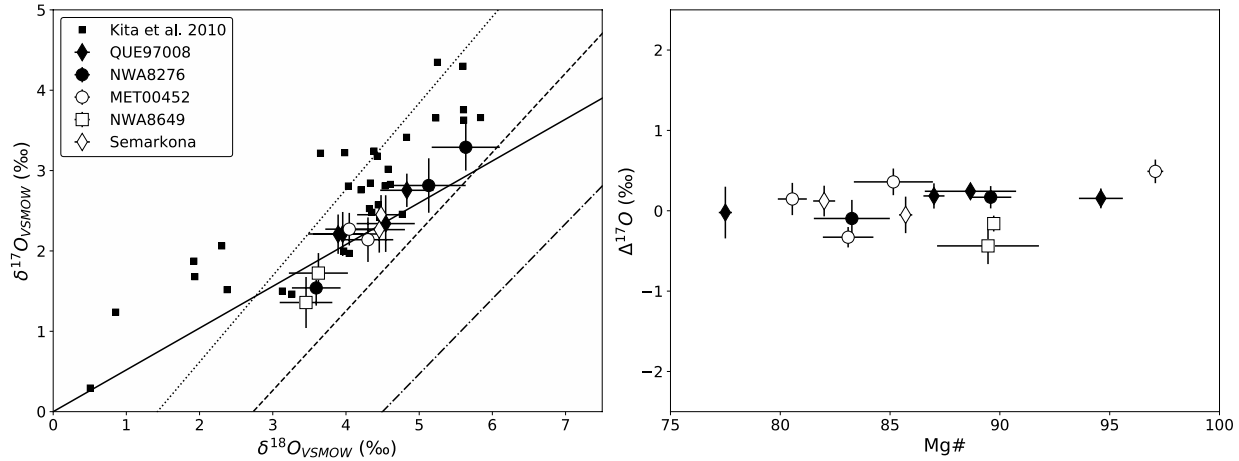
Fig. 5: Composition of plagioclase grains analyzed from the selected chondrules. a) Anorthite content (calculated as  $\text{Ca} / (\text{Ca} + \text{Na} + \text{K})$  mol%) vs excess silica ( $\text{Si}_4\text{O}_8$ ); b) Anorthite content vs  $\text{MgO}$  (wt%) content.



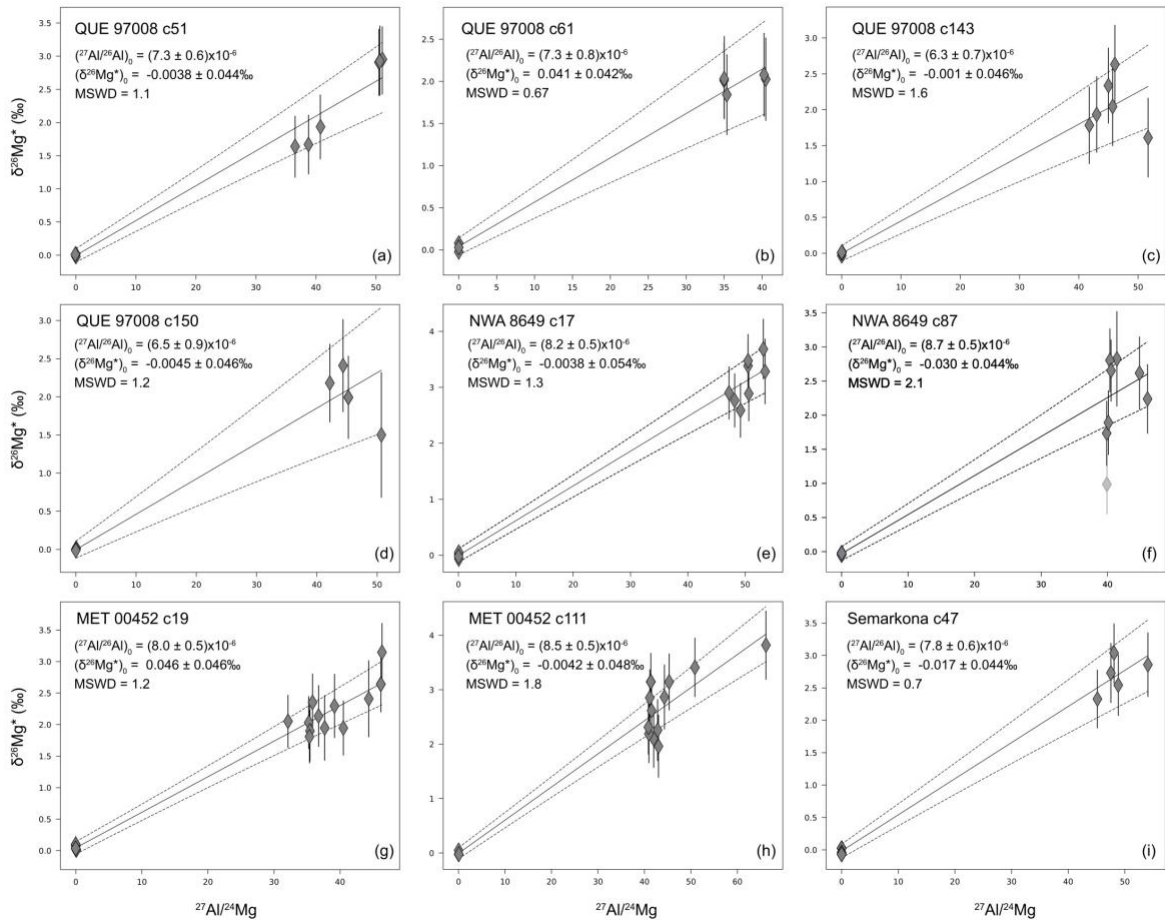
1178  
1179 Fig. 6: Individual oxygen three-isotope analyses of of 7 studied chondrules. a) QUE 97008 c51, b) NWA  
1180 8276 c87, c) Semarkona c47, d) Semarkona c34, e) MET 00452 c19, f) MET 00452 c11, g) NWA  
1181 8649 c17. Symbols of minerals are as follows, dots: olivine, diamonds: pyroxene and squares: plagioclase. Error  
1182 bars represent 2SD of bracketing standards. Transparent symbols represent data not used for the  
1183 computation of the host chondrule values.



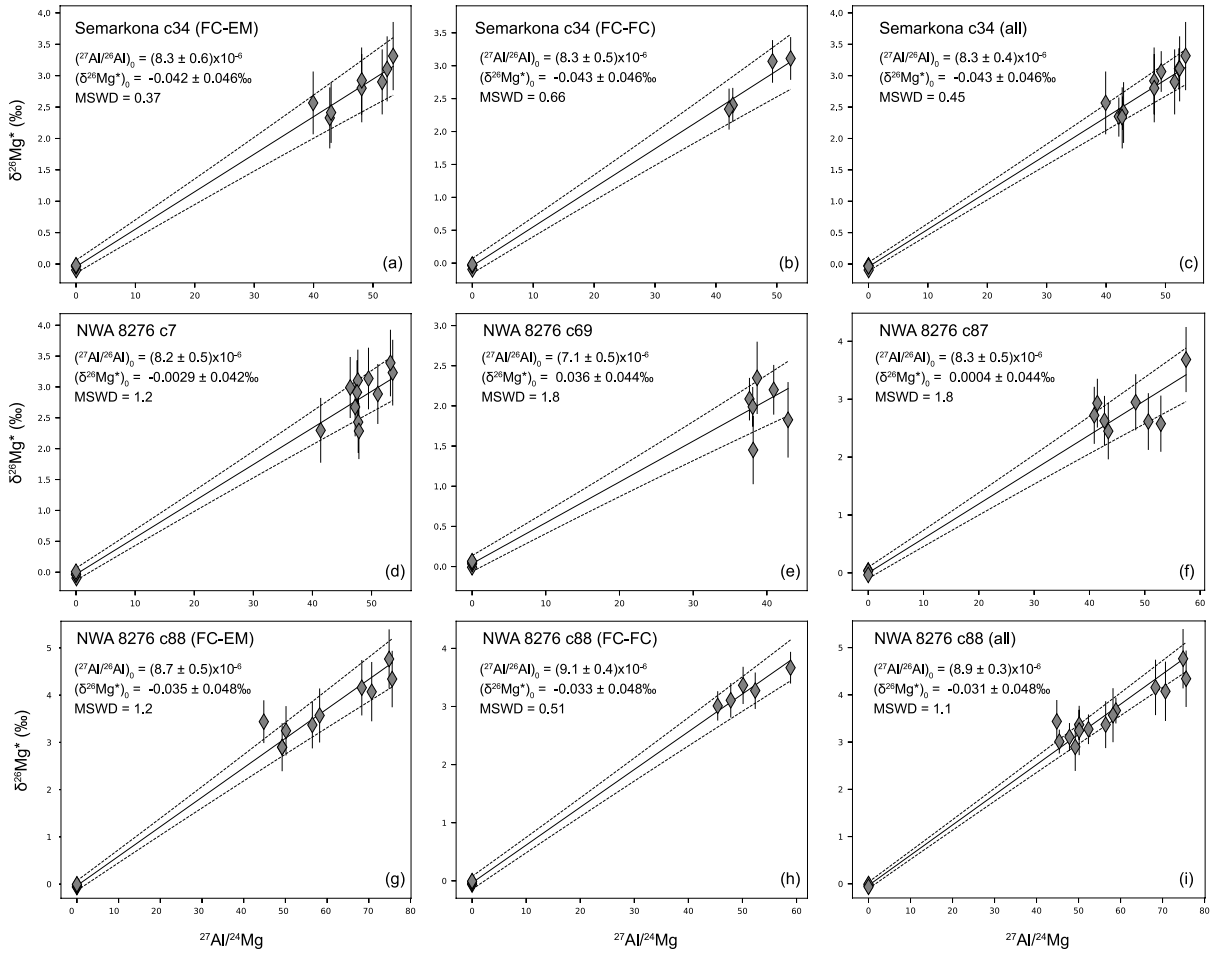
1184  
1185 Fig. 7: Individual oxygen three-isotope analyses of remaining 6 chondrules studied. a) NWA 8276 c7, b)  
1186 NWA 8276 c88, c) QUE 97008 c61, d) QUE 97008 c143, e) QUE 97008 c150, f) NWA 8276 c87. Symbols  
1187 of minerals are the same as in those Fig. 6. Error bars represent 2SD of bracketing standards. Transparent  
1188 symbols represent data not used for the computation of the host chondrule values.



1189  
1190 Fig. 8: a) Host chondrule  $\delta^{18}\text{O}$  vs  $\delta^{17}\text{O}$  plot of 13 chondrules, except for NWA 1191  
1192 8276 c69 (see text for explanation). Error bars represent 2SE. b) Host chondrule  $\Delta^{17}\text{O}$  values vs Mg# of olivine/pyroxene. Error  
1193 bars represent 2SE.

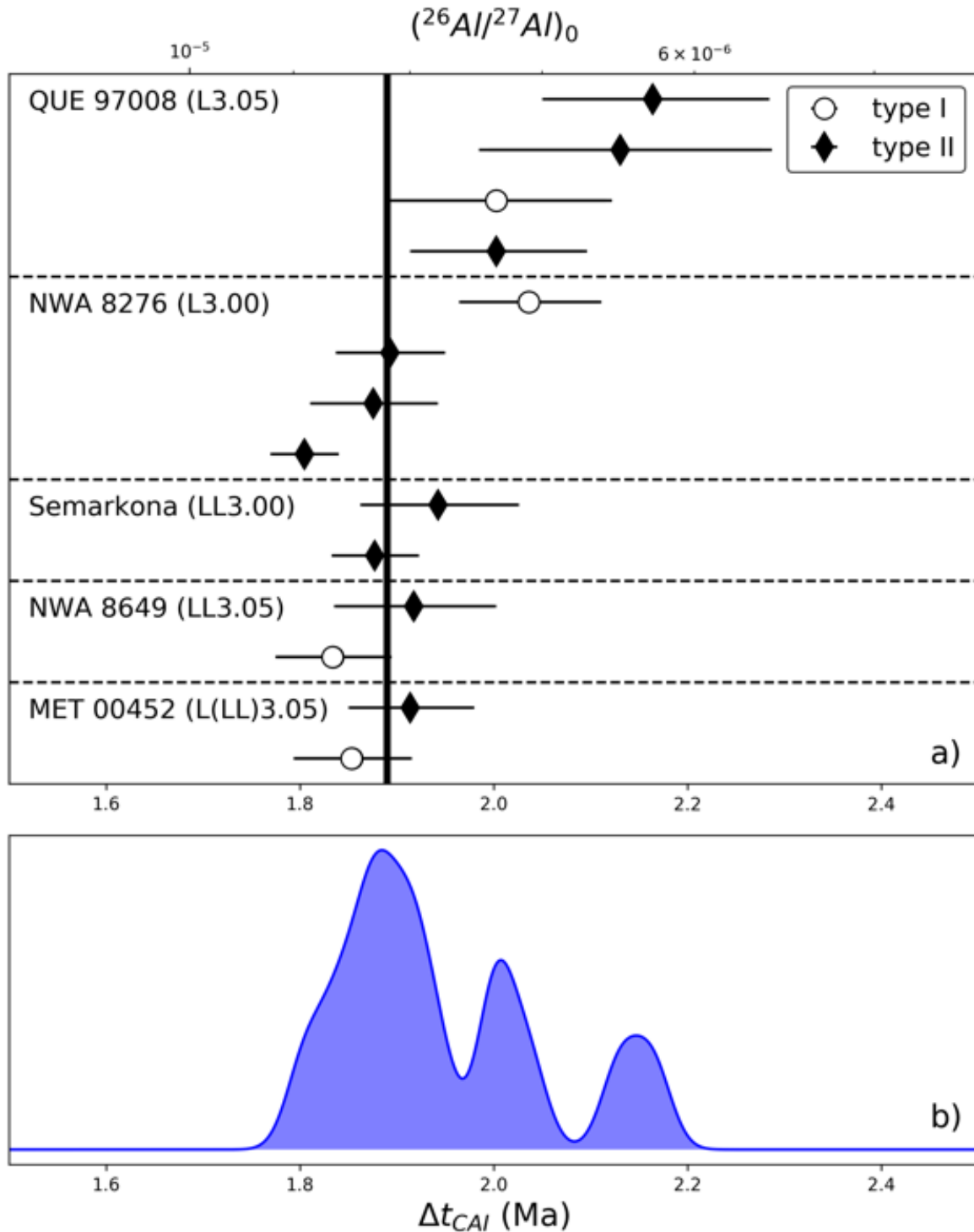


1194  
1195 Fig. 9: Internal isochron regression for 9 studied chondrules in this study. Error bars represent 2SE. The  
1196 solid lines represent the regressions and dash lines are 95% confidence interval on the fit. Uncertainties for  
1197  $(^{26}\text{Al}/^{27}\text{Al})_0$  and  $(\delta^{26}\text{Mg}^*)_0$  are 95% confidence level.



1198

1199 Fig. 10: Internal isochron regression for 5 studied chondrules in this study, including two that were analyzed  
1200 for MCFC (FC-FC) and FC-EM modes. Error bars represent 2SE. The solid lines represent the regressions  
1201 and dash lines are 95% confidence interval on the fit. Uncertainties for  $(^{26}\text{Al}/^{27}\text{Al})_0$  and  $(\delta^{26}\text{Mg}^*)_0$  are 95%  
1202 confidence level.



1203  
 1204 Fig. 11: a) Compilation of initial  $^{26}\text{Al}/^{27}\text{Al}$  ratios (upper axis)  
 1205 computed from internal isochron for each chondrule from this study.  
 1206 Error bars shown are uncertainties  
 1207 from isochron regression in Figs. 10-11. Chondrule type are as follows: type-I (open dots)  
 1208 and type-II (filled diamonds). The thick black line represents the weighted mean age for all chondrules. b) Kernel density  
 function for the distribution of all ages from this study.

1209  
1210

Table 1. Average major and minor elements for olivine composition determined with EPMA

|                                | QUE 97008, 12 |        |       |        | MET 00452, 16 |        | NWA 8649 |        | NWA 8276 |       |       |                           | Semarkona                     |       |
|--------------------------------|---------------|--------|-------|--------|---------------|--------|----------|--------|----------|-------|-------|---------------------------|-------------------------------|-------|
|                                | c51           | c61    | c143  | c150   | c19           | c111   | c17      | c87    | c7       | c69   | c87   | c <sup>88</sup><br>(core) | c <sup>88</sup><br>(rim inc.) | c47   |
| SiO <sub>2</sub>               | 39.73         | 41.11  | 39.51 | 37.93  | 39.19         | 40.16  | 40.85    | 40.18  | 39.57    | 41.30 | 38.80 | 37.88                     | 38.35                         | 39.43 |
| TiO <sub>2</sub>               | 0.02          | 0.07   | 0.01  | 0.04   | 0.02          | 0.02   | 0.05     | 0.06   | 0.03     | 0.08  | 0.01  | 0.03                      | 0.01                          | 0.04  |
| Al <sub>2</sub> O <sub>3</sub> | 0.10          | 0.10   | 0.16  | 0.04   | 0.09          | 0.07   | 0.03     | 0.08   | 0.15     | 0.15  | 0.21  | 0.03                      | 0.03                          | 0.05  |
| MgO                            | 46.75         | 52.91  | 44.01 | 40.34  | 44.16         | 49.19  | 52.09    | 49.08  | 45.49    | 54.38 | 43.96 | 39.26                     | 42.03                         | 45.49 |
| FeO                            | 12.72         | 5.38   | 15.17 | 20.89  | 15.81         | 10.19  | 7.26     | 10.02  | 14.12    | 2.91  | 15.94 | 21.36                     | 18.09                         | 13.52 |
| CaO                            | 0.22          | 0.25   | 0.22  | 0.20   | 0.26          | 0.19   | 0.18     | 0.22   | 0.22     | 0.24  | 0.30  | 0.24                      | 0.24                          | 0.24  |
| Na <sub>2</sub> O              | 0.00          | -0.01  | 0.03  | -0.01  | 0.00          | 0.00   | -0.02    | -0.01  | 0.00     | 0.00  | 0.00  | 0.00                      | 0.00                          | 0.00  |
| MnO                            | 0.20          | 0.09   | 0.32  | 0.31   | 0.21          | 0.22   | 0.16     | 0.18   | 0.20     | 0.05  | 0.17  | 0.35                      | 0.30                          | 0.25  |
| Cr <sub>2</sub> O <sub>3</sub> | 0.61          | 0.55   | 0.55  | 0.29   | 0.61          | 0.52   | 0.30     | 0.59   | 0.56     | 0.59  | 0.45  | 0.49                      | 0.47                          | 0.56  |
| Total                          | 100.33        | 100.45 | 99.98 | 100.02 | 100.36        | 100.56 | 100.89   | 100.40 | 100.33   | 99.70 | 99.84 | 99.64                     | 99.53                         | 99.57 |
| Si                             | 0.989         | 0.988  | 1.00  | 0.984  | 0.990         | 0.986  | 0.984    | 0.987  | 0.991    | 0.989 | 0.985 | 0.990                     | 0.988                         | 0.990 |
| Al                             | 0.003         | 0.003  | 0.00  | 0.001  | 0.003         | 0.002  | 0.001    | 0.002  | 0.004    | 0.004 | 0.006 | 0.001                     | 0.001                         | 0.001 |
| Mg                             | 1.735         | 1.896  | 1.66  | 1.560  | 1.663         | 1.800  | 1.872    | 1.798  | 1.698    | 1.942 | 1.665 | 1.530                     | 1.614                         | 1.703 |
| Fe                             | 0.265         | 0.108  | 0.32  | 0.453  | 0.334         | 0.209  | 0.146    | 0.206  | 0.296    | 0.058 | 0.339 | 0.467                     | 0.390                         | 0.284 |
| Ca                             | 0.006         | 0.007  | 0.01  | 0.006  | 0.007         | 0.005  | 0.005    | 0.006  | 0.006    | 0.006 | 0.008 | 0.007                     | 0.007                         | 0.006 |
| Mn                             | 0.004         | 0.002  | 0.01  | 0.007  | 0.005         | 0.005  | 0.003    | 0.004  | 0.004    | 0.001 | 0.004 | 0.008                     | 0.007                         | 0.005 |
| Cr                             | 0.012         | 0.010  | 0.01  | 0.006  | 0.012         | 0.010  | 0.006    | 0.011  | 0.011    | 0.011 | 0.009 | 0.010                     | 0.010                         | 0.006 |
| Sum Oct                        | 2.022         | 2.022  | 2.00  | 2.032  | 2.021         | 2.029  | 2.031    | 2.025  | 2.016    | 2.018 | 2.024 | 2.022                     | 2.027                         | 1.987 |
| Fo <sup>a</sup>                | 86.8          | 94.6   | 83.8  | 77.5   | 83.3          | 89.6   | 92.7     | 89.7   | 85.2     | 97.1  | 83.1  | 76.6                      | 80.6                          | 85.7  |

<sup>a</sup>Fo = Mg / (Mg + Fe) mol%1211  
1212  
1213

Table 2. Average major and minor elements for pyroxene composition determined with EPMA

|                                | QUE 97008, 12 |       |       | MET 00452, 16 |        |        | NWA 8649      |               | NWA 8276 |       |       |       |
|--------------------------------|---------------|-------|-------|---------------|--------|--------|---------------|---------------|----------|-------|-------|-------|
|                                | c51           | c61   | c143  | c150          | c19    | c111   | c17<br>(core) | c17<br>(rims) | c87      | c7    | c69   | c88   |
| SiO <sub>2</sub>               | 54.18         | 54.43 | 51.78 | 52.60         | 55.58  | 56.09  | 55.04         | 56.35         | 54.91    | 52.64 | 55.96 | 55.63 |
| TiO <sub>2</sub>               | 0.19          | 0.55  | 0.58  | 0.13          | 0.13   | 0.14   | 0.16          | 0.19          | 0.15     | 0.51  | 0.41  | 0.04  |
| Al <sub>2</sub> O <sub>3</sub> | 2.75          | 2.71  | 2.55  | 2.16          | 1.58   | 1.53   | 1.98          | 1.74          | 2.56     | 2.57  | 1.91  | 0.40  |
| MgO                            | 30.04         | 29.30 | 22.93 | 27.45         | 32.47  | 34.23  | 31.57         | 34.35         | 32.83    | 25.72 | 34.14 | 31.40 |
| FeO                            | 8.20          | 4.94  | 14.43 | 12.36         | 7.22   | 5.86   | 7.81          | 4.78          | 5.75     | 10.76 | 2.01  | 10.31 |
| CaO                            | 2.66          | 6.65  | 5.26  | 2.60          | 1.57   | 1.28   | 1.50          | 1.77          | 1.86     | 5.23  | 3.75  | 0.56  |
| Na <sub>2</sub> O              | 0.01          | 0.01  | 0.00  | 0.01          | 0.00   | 0.00   | 0.00          | 0.00          | -0.01    | 0.00  | 0.00  | 0.00  |
| MnO                            | 0.24          | 0.13  | 0.52  | 0.35          | 0.25   | 0.21   | 0.48          | 0.14          | 0.16     | 0.30  | 0.03  | 0.21  |
| Cr <sub>2</sub> O <sub>3</sub> | 1.52          | 1.08  | 1.09  | 1.18          | 1.31   | 1.00   | 1.19          | 0.84          | 1.48     | 1.24  | 1.04  | 0.78  |
| Total                          | 99.80         | 99.80 | 99.16 | 98.84         | 100.09 | 100.32 | 99.74         | 100.17        | 99.67    | 98.96 | 99.27 | 99.32 |
| Si                             | 1.926         | 1.921 | 1.921 | 1.924         | 1.950  | 1.946  | 1.944         | 1.947         | 1.927    | 1.923 | 1.941 | 1.980 |
| Ti                             | 0.005         | 0.015 | 0.017 | 0.004         | 0.003  | 0.004  | 0.004         | 0.005         | 0.004    | 0.014 | 0.011 | 0.001 |
| Al                             | 0.115         | 0.113 | 0.112 | 0.093         | 0.065  | 0.063  | 0.082         | 0.071         | 0.106    | 0.110 | 0.078 | 0.017 |
| Sum                            | 2.046         | 2.049 | 2.049 | 2.021         | 2.019  | 2.012  | 2.030         | 2.023         | 2.036    | 2.047 | 2.030 | 1.998 |
| Mg                             | 1.591         | 1.542 | 1.265 | 1.497         | 1.699  | 1.770  | 1.662         | 1.769         | 1.717    | 1.400 | 1.765 | 1.666 |
| Fe                             | 0.244         | 0.146 | 0.449 | 0.378         | 0.212  | 0.170  | 0.231         | 0.139         | 0.169    | 0.329 | 0.058 | 0.307 |
| Ca                             | 0.101         | 0.251 | 0.211 | 0.102         | 0.059  | 0.048  | 0.057         | 0.066         | 0.070    | 0.205 | 0.140 | 0.021 |
| Mn                             | 0.007         | 0.004 | 0.016 | 0.011         | 0.007  | 0.006  | 0.015         | 0.004         | 0.005    | 0.009 | 0.001 | 0.006 |
| Cr                             | 0.043         | 0.030 | 0.032 | 0.034         | 0.036  | 0.027  | 0.033         | 0.023         | 0.041    | 0.036 | 0.029 | 0.022 |
| Na                             | 0.001         | 0.001 | 0.000 | 0.001         | 0.000  | 0.000  | 0.000         | 0.000         | -0.001   | 0.000 | 0.000 | 0.000 |
| Sum Oct                        | 1.987         | 1.973 | 1.973 | 2.022         | 2.013  | 2.021  | 1.997         | 2.001         | 2.001    | 1.979 | 1.993 | 2.023 |
| Mg# <sup>a</sup>               | 86.7          | 91.4  | 73.5  | 79.8          | 88.9   | 91.2   | 87.8          | 92.7          | 91.1     | 81.0  | 96.8  | 84.5  |
| En <sup>b</sup>                | 81.9          | 79.4  | 65.2  | 75.3          | 85.9   | 88.8   | 84.6          | 89.5          | 87.6     | 72.1  | 89.9  | 83.3  |
| Wo <sup>c</sup>                | 5.2           | 12.9  | 10.9  | 5.1           | 3.0    | 2.4    | 2.9           | 3.3           | 3.6      | 10.5  | 7.1   | 1.1   |

<sup>a</sup>Mg# = Mg / (Mg + Fe) mol%. <sup>b</sup>En = Mg / (Mg + Fe + Ca) mol%. <sup>c</sup>Wo = Ca / (Mg + Fe + Ca) mol%

1219

Table 3: Average major and minor elements for plagioclase composition determined with EPMA

|  | MET 00452, 16 |        | NWA 8649 |       | QUE 97008, 12 |       | Semarkona |       | NWA 8276 |       |       |        |       |
|--|---------------|--------|----------|-------|---------------|-------|-----------|-------|----------|-------|-------|--------|-------|
|  | c19           | c111   | c17      | c87   | c51           | c61   | c143      | c150  | c47      | c7    | c69   | c87    | c88   |
| SiO <sub>2</sub>   | 45.46         | 46.90  | 44.73    | 44.87 | 45.86         | 46.13 | 46.55     | 45.72 | 44.88    | 45.59 | 45.32 | 44.84  | 44.28 |
| TiO <sub>2</sub>   | 0.02          | 0.02   | 0.03     | 0.02  | 0.03          | 0.02  | 0.01      | 0.02  | 0.04     | 0.01  | 0.05  | 0.02   | 0.04  |
| Al <sub>2</sub> O <sub>3</sub>                           | 33.28         | 32.47  | 34.44    | 33.64 | 32.91         | 32.78 | 32.61     | 32.80 | 33.73    | 33.27 | 33.53 | 33.61  | 33.86 |
| MgO  | 0.83          | 0.87   | 0.64     | 0.75  | 0.74          | 0.98  | 0.78      | 0.74  | 0.72     | 0.80  | 0.85  | 0.73   | 0.61  |
| FeO  | 0.63          | 0.85   | 0.32     | 0.52  | 0.85          | 0.43  | 1.04      | 0.96  | 0.90     | 0.81  | 0.31  | 1.34   | 0.90  |
| CaO  | 19.39         | 19.01  | 19.13    | 18.75 | 18.94         | 19.32 | 18.70     | 18.91 | 19.25    | 19.27 | 19.35 | 19.21  | 19.34 |
| Na <sub>2</sub> O  | 0.23          | 0.24   | 0.73     | 0.77  | 0.42          | 0.17  | 0.40      | 0.36  | 0.05     | 0.15  | 0.14  | 0.29   | 0.05  |
| K <sub>2</sub> O   | 0.00          | 0.00   | 0.00     | 0.00  | 0.00          | -0.01 | 0.00      | 0.00  | 0.00     | 0.00  | 0.01  | 0.03   | 0.03  |
| MnO  | 0.00          | -0.01  | 0.01     | 0.00  | 0.01          | 0.01  | 0.00      | -0.01 | 0.02     | 0.01  | 0.00  | 0.02   | 0.02  |
| Total  | 99.84         | 100.37 | 100.04   | 99.33 | 99.76         | 99.84 | 100.12    | 99.51 | 99.60    | 99.93 | 99.55 | 100.08 | 99.13 |
| Si   | 2.108         | 2.158  | 2.071    | 2.091 | 2.127         | 2.134 | 2.150     | 2.127 | 2.088    | 2.112 | 2.103 | 2.083  | 2.072 |
| Al   | 1.818         | 1.761  | 1.879    | 1.848 | 1.799         | 1.787 | 1.775     | 1.799 | 1.849    | 1.816 | 1.834 | 1.840  | 1.868 |
| Ca   | 0.963         | 0.938  | 0.949    | 0.936 | 0.941         | 0.958 | 0.925     | 0.942 | 0.959    | 0.957 | 0.962 | 0.956  | 0.970 |
| Na   | 0.021         | 0.021  | 0.065    | 0.070 | 0.037         | 0.015 | 0.036     | 0.033 | 0.004    | 0.014 | 0.012 | 0.026  | 0.005 |
| K  | 0.000         | 0.000  | 0.000    | 0.000 | 0.000         | 0.000 | 0.000     | 0.000 | 0.000    | 0.000 | 0.000 | 0.002  | 0.002 |
| Mg   | 0.058         | 0.060  | 0.044    | 0.052 | 0.051         | 0.068 | 0.054     | 0.051 | 0.050    | 0.056 | 0.059 | 0.051  | 0.042 |
| Fe   | 0.025         | 0.033  | 0.013    | 0.020 | 0.033         | 0.017 | 0.040     | 0.037 | 0.035    | 0.031 | 0.012 | 0.052  | 0.035 |
| Mn   | 0.000         | 0.000  | 0.000    | 0.000 | 0.000         | 0.000 | 0.000     | 0.000 | 0.001    | 0.000 | 0.000 | 0.001  | 0.001 |
| End-Member proportions                                   |               |        |          |       |               |       |           |       |          |       |       |        |       |
| Ca(Fe,Mg,Mn)Si <sub>3</sub> O <sub>8</sub>               | 0.069         | 0.080  | 0.033    | 0.046 | 0.071         | 0.078 | 0.071     | 0.070 | 0.059    | 0.070 | 0.060 | 0.068  | 0.056 |
| KAlSi <sub>3</sub> O <sub>8</sub>                        | 0.000         | 0.000  | 0.000    | 0.000 | 0.000         | 0.000 | 0.000     | 0.000 | 0.000    | 0.000 | 0.001 | 0.001  | 0.002 |
| NaAlSi <sub>3</sub> O <sub>8</sub>                       | 0.016         | 0.021  | 0.049    | 0.056 | 0.036         | 0.014 | 0.032     | 0.029 | 0.002    | 0.013 | 0.011 | 0.018  | 0.004 |
| CaAl <sub>2</sub> Si <sub>2</sub> O <sub>8</sub>         | 0.891         | 0.857  | 0.906    | 0.883 | 0.870         | 0.879 | 0.852     | 0.870 | 0.899    | 0.885 | 0.901 | 0.884  | 0.912 |
| (Fe,Mg,Mn)Al <sub>2</sub> Si <sub>2</sub> O <sub>8</sub> | 0.010         | 0.012  | 0.008    | 0.012 | 0.012         | 0.008 | 0.019     | 0.015 | 0.024    | 0.016 | 0.010 | 0.026  | 0.019 |
| □Si <sub>4</sub> O <sub>8</sub>                          | 0.013         | 0.028  | 0.000    | 0.000 | 0.011         | 0.021 | 0.024     | 0.015 | 0.015    | 0.015 | 0.017 | 0.001  | 0.007 |
| An <sup>a</sup>  | 97.9          | 97.8   | 93.6     | 93.1  | 96.2          | 98.5  | 96.3      | 96.7  | 99.6     | 98.6  | 98.7  | 97.2   | 99.4  |

<sup>a</sup> An = Ca / (Ca + Na +K) mol%

1220

1221

1222

1223

Table 4. Host oxygen three isotope ratios of anorthite bearing chondrules.

| Chondrule        | n | Type   | $\delta^{18}\text{O}$ | Unc. | $\delta^{17}\text{O}$ | Unc. | $\Delta^{17}\text{O}$ | Unc. | Mg# <sup>a</sup> |
|------------------|---|--------|-----------------------|------|-----------------------|------|-----------------------|------|------------------|
| <i>QUE 97008</i> |   |        |                       |      |                       |      |                       |      |                  |
| c51              | 7 | II-PO  | 3.89                  | 0.34 | 2.21                  | 0.25 | 0.18                  | 0.16 | 87               |
| c61              | 7 | I-POP  | 3.96                  | 0.47 | 2.21                  | 0.27 | 0.15                  | 0.12 | 95               |
| c143             | 8 | II-PO  | 4.83                  | 0.36 | 2.75                  | 0.21 | 0.24                  | 0.09 | 84               |
| c150             | 8 | II-POP | 4.54                  | 0.40 | 2.34                  | 0.35 | -0.02                 | 0.32 | 87               |
| <i>MET 00452</i> |   |        |                       |      |                       |      |                       |      |                  |
| c19              | 7 | II-PO  | 4.30                  | 0.35 | 2.14                  | 0.28 | -0.10                 | 0.23 | 83               |
| c111             | 8 | II-POP | 4.04                  | 0.33 | 2.27                  | 0.20 | 0.17                  | 0.14 | 90               |
| <i>Semarkona</i> |   |        |                       |      |                       |      |                       |      |                  |
| c34              | 8 | II-POP | 4.48                  | 0.33 | 2.45                  | 0.24 | 0.12                  | 0.19 | 82               |
| c47              | 8 | II-PO  | 4.45                  | 0.35 | 2.26                  | 0.29 | -0.05                 | 0.23 | 86               |
| <i>NWA 8649</i>  |   |        |                       |      |                       |      |                       |      |                  |
| c17              | 8 | I-PP   | 3.45                  | 0.36 | 1.36                  | 0.32 | -0.44                 | 0.23 | 93               |
| c87              | 6 | II-PO  | 3.62                  | 0.40 | 1.72                  | 0.25 | -0.16                 | 0.10 | 90               |
| <i>NWA 8276</i>  |   |        |                       |      |                       |      |                       |      |                  |
| c7               | 6 | II-PO  | 5.64                  | 0.47 | 3.29                  | 0.29 | 0.36                  | 0.17 | 85               |
| c69              | 6 | I-POP  |                       |      |                       |      | 0.49                  | 0.15 | 97               |
| c87              | 8 | II-PO  | 3.59                  | 0.33 | 1.54                  | 0.22 | -0.33                 | 0.13 | 83               |
| c88              | 8 | II-POP | 5.13                  | 0.51 | 2.81                  | 0.34 | 0.15                  | 0.20 | 80               |

1224

<sup>a</sup>Mg# = Mg / (Mg + Fe) mole%

1225

1226

Table 5. Summary of Al-Mg chronology of anorthite-bearing chondrules.

| Chondrule        | n  | Type   | MSWD | slope  | unc.   | $\delta^{26}\text{Mg}_0$<br>(‰) | unc.  | $(^{26}\text{Al}/^{27}\text{A})$<br>$\times 10^{-6}$ | unc.<br>$\times 10^{-6}$ | $\Delta t_{\text{CAIs}}$<br>(Ma) | unc. |
|------------------|----|--------|------|--------|--------|---------------------------------|-------|--|--------------------------|----------------------------------|------|
| <i>QUE 97008</i> |    |        |      |        |        |                                 |       |  |                          |                                  |      |
| c51              | 10 | II-PO  | 1.1  | 0.0526 | 0.0046 | -0.004                          | 0.044 | 7.33   | 0.64                     | 2.00                             | 0.09 |
| c61              | 9  | I-POP  | 0.67 | 0.0526 | 0.0058 | 0.041                           | 0.042 | 7.33   | 0.81                     | 2.00                             | 0.11 |
| c143             | 10 | II-PO  | 1.6  | 0.0449 | 0.0050 | -0.001                          | 0.046 | 6.26   | 0.70                     | 2.16                             | 0.11 |
| c150             | 8  | II-POP | 1.2  | 0.0464 | 0.0066 | -0.005                          | 0.046 | 6.46   | 0.92                     | 2.13                             | 0.15 |
| <i>MET 00452</i> |    |        |      |        |        |                                 |       |  |                          |                                  |      |
| c19              | 16 | II-PO  | 1.2  | 0.0574 | 0.0036 | 0.046                           | 0.046 | 8.00   | 0.50                     | 1.91                             | 0.06 |
| c111             | 16 | II-POP | 1.8  | 0.0609 | 0.0036 | -0.004                          | 0.048 | 8.48   | 0.50                     | 1.85                             | 0.06 |
| <i>Semarkona</i> |    |        |      |        |        |                                 |       |  |                          |                                  |      |
| c47              | 9  | II-POP | 0.7  | 0.0558 | 0.0044 | -0.017                          | 0.044 | 7.77   | 0.61                     | 1.94                             | 0.08 |
| c34 (FC-EM)      | 12 | II-PO  | 0.37 | 0.0598 | 0.0040 | -0.042                          | 0.046 | 8.33   | 0.56                     | 1.87                             | 0.07 |
| c34 (FC-FC)      | 8  |        | 0.66 | 0.0594 | 0.0034 | -0.043                          | 0.046 | 8.28   | 0.47                     | 1.88                             | 0.06 |
| c34 (all)        | 16 |        | 0.45 | 0.0595 | 0.0026 | -0.043                          | 0.046 | 8.29   | 0.36                     | 1.88                             | 0.04 |
| <i>NWA 8649</i>  |    |        |      |        |        |                                 |       |  |                          |                                  |      |
| c17              | 12 | I-PP   | 1.3  | 0.0621 | 0.0038 | -0.004                          | 0.054 | 8.65   | 0.50                     | 1.83                             | 0.06 |
| c87              | 11 | II-PO  | 2.1  | 0.0572 | 0.0046 | -0.030                          | 0.044 | 7.97   | 0.64                     | 1.92                             | 0.08 |
| <i>NWA 8276</i>  |    |        |      |        |        |                                 |       |  |                          |                                  |      |
| c7               | 15 | II-PO  | 1.2  | 0.0586 | 0.0032 | -0.003                          | 0.042 | 8.16   | 0.45                     | 1.89                             | 0.06 |
| c69              | 10 | I-POP  | 1.8  | 0.0509 | 0.0036 | 0.036                           | 0.044 | 7.09   | 0.50                     | 2.04                             | 0.07 |
| c87              | 10 | II-PO  | 1.8  | 0.0596 | 0.0038 | 0.000                           | 0.044 | 8.30   | 0.53                     | 1.88                             | 0.06 |
| c88 (FC-EM)      | 13 | II-POP | 1.2  | 0.0624 | 0.0032 | -0.035                          | 0.048 | 8.69   | 0.45                     | 1.83                             | 0.05 |
| c88 (FC-FC)      | 9  |        | 0.51 | 0.0650 | 0.0026 | -0.033                          | 0.048 | 9.06   | 0.36                     | 1.79                             | 0.04 |
| c88 (all)        | 18 |        | 1.1  | 0.0639 | 0.0022 | -0.031                          | 0.048 | 8.90   | 0.31                     | 1.80                             | 0.04 |